



UNIVERSITY
OF TRENTO - Italy

DEPARTMENT OF INDUSTRIAL ENGINEERING

XXIV cycle

Doctoral School in Materials Science and Engineering

Co-sintering of a metal injection overmolded bi-metallic part

Marco Cazzoli

April 2015

Co-sintering of a metal injection overmolded bi-metallic part

Marco Cazzoli

E-mail: marco.cazzoli@unitn.it

Tutors:

Prof. Alberto Molinari

Department of Industrial
Engineering

University of Trento, Italy

Ph.D. Commission:

Prof. José Manuel Torralba Castelló,
IMDEA Materials Institute
University Carlos III de Madrid, Spain.

Prof. Giovanni Straffelini,
Department of Industrial Engineering
University of Trento, Italy.

Prof. Yves Leterrier,
Laboratoire de Technologie des
Composites et Polymères,
*Ecole Polytechnique Fédérale
de Lausanne, Swiss.*

Dott.ssa Antonietta Guagliardi
Institute of Crystallography,
IC-CNR.

University of Trento,
Department of Industrial Engineering

April 2015

Summary

Introduction.....	5
1.0 Metal injection molding	8
1.1 The MIM process	10
1.1.1 Powders used in the MIM process	12
1.1.2 Binders for the MIM feedstock.....	18
1.1.3 Injection molding.....	21
1.1.4 Debinding.....	25
1.1.5 Sintering.....	27
1.2 Two-materials injection moulding.....	30
2.0 2C-mim. Scientific context.....	35
3.0 Experimental procedures	41
3.1 Sample production	41
3.2 Metallographic preparation and analysis.....	43
3.3 Scanning Electron Microscope observation and EDXS analysis	45
3.4 Mechanical tests.....	46
3.5 Dilatometry test.....	47
3.6 Corrosion tests.....	50

4.0 Results and discussion	51
4.1 430 Prealloy – 316L Prealloy route.....	51
4.1.1 Powder analysis	51
4.1.2 Dilatometry tests	55
4.2 430 Prealloy – 316L Master Alloy route	58
4.2.1 Powder analysis	59
4.2.2 Dilatometry tests	61
4.3 430 Master Alloy – 316L Master Alloy route.....	64
4.3.1 Powder analysis	64
4.3.2 Dilatometry test.....	66
4.4 Calculation of the ACSI	69
4.5 Dimensional changes	71
4.6 Microstructure.....	76
4.7 Characterization of the interface constituent	79
4.8 Thermo Calc and Dictra simulation	81
4.9 Mechanical properties.....	88
4.10 Corrosion resistance	99
5.0 Conclusions.....	105
6.0 Bibliography.....	109

Introduction

Metal Injection Molding (MIM) is a suitable technology for the mass production of many automotive metal parts and components. Intricate geometry, good tolerances, very low porosity and mechanical properties comparable to the cast alloys of the same composition are very attractive. The study proposed in this work is within an industrial project, in cooperation with Mimest SpA, aimed at developing the production of a bimetallic component. This component is a valve used in fuel injection system to open and close the fuel flux and it is moved by the magnetic field generated by a solenoid. At the moment this component is produced by turning an austenitic stainless steel disc to obtain the final geometry and also the seat for a magnet that is used to make the part sensible to the induced magnetic field. A cost and time reducing solution for the coupling of two different metals can be the “two component powder injection molding” (2C-MIM). The component was partially redesigned to exploit the potentiality of this technique. The adoption of a ferromagnetic steel, (AISI 430) makes the part sensible to the magnetic field but the force necessary to move it can be decreased by substituting part of the volume with a paramagnetic austenite stainless steel (AISI316L).

The aim of the work is the study of the feasibility of the process to obtain a defect less part, with special attention on the sintering process. The co-sintering of the two metals creates an interface that can be a weak point of the component from different points of view: matching of the dimensional change on sintering, mechanical properties and corrosion resistance.

The dimensional changes on sintering were investigated by dilatometry, to evaluate the differences in shrinkage and shrinkage rate during the heating and the isothermal sintering steps. Different feedstocks, based on different powders of the two steels, were investigated. For each feedstock combination an Apparent Co-sintering Index (ACSI) was calculated, that should be minimized to avoid delamination and cracks at the interface. To verify the reliability of these measurements, part prototypes were produced. CMM measures on the parts freely sintered and of the co-sintered component were also made to confirm the dilatometry results. Once a part free from cracks or delamination was obtained, the attention was focused on the study of the microstructure created in the interface between the two metals. The microstructure was investigated by metallographic analysis and EDXS line profiles. The results were compared to Thermocalc and Dictra simulation.

In the last part of the work, tensile tests and electrochemical corrosion tests were carried out. To verify the properties of the microstructural constituent produced at the interface, specific specimens were produced by mixing the two feedstocks. Tensile tests were carried out using the ferritic and the austenitic steels as a reference, and the effect of the destabilization of austenite, due to migration of Ni and Mo towards the ferritic stainless steel, was investigated. Of course the use of a stainless steel is related to the possibility to have a passivation of the metal by the formation of a protective oxide layer. This passivity must remain also for the interface constituents; to prove it the potentiodynamic curves were studied again on specific specimens, using the curves base steels as a reference.

1.0 Metal injection molding

Powder Injection Molding (PIM) is a technology born in the 70's that can be divided in two fields . Metal Injection Molding (MIM) when the load inside the polymeric binder is made of metal particles and Ceramic Injection Molding (CIM) when the load is composed of ceramic particles [1, 2]. In MIM the purpose is molding metal particles in a specific geometry and sinter them to obtain an almost full density alloy. In this way MIM can be seen as an hybrid technology where two fields of Material Science and Engineering are joined to catch the best advantages from each one in order to have a synergic evolution. Polymer science, in the specific the plastic injection molding, and powder metallurgy process are molten in a single technique. In the field of powder metallurgy (PM) MIM is, since the last twenty years, one of the most growing techniques . This technology is able to produce net shape components with extremely complex geometry. Most of the parts produced are used in common sectors of the industry such as automotive, electronic products, armaments and so on. MIM parts are now used by all of us in our everyday life. The reduction of costs and processing time makes the MIM process win against old technique such as investment casting, the technology that is more similar to MIM than others. Quality of the microstructure and pores

shape together with high production volume is the ace in the hole that makes MIM interesting; also the possibility to produce extreme complex geometry is extremely advantageous respect to other PM techniques. The worldwide situation based in percentage of global sale in 2012 is represented in figure 1 :

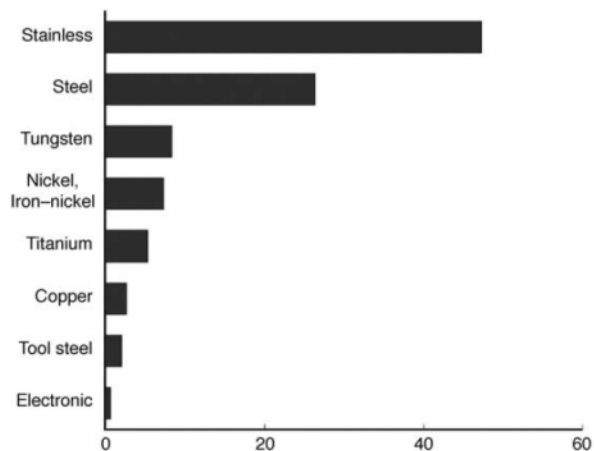


Figure 1 Percentage of global sale divided by processed metal or alloy [1]

MIM is limited by some restrictions related to the mass and geometry of the parts. It's necessary to limit some dimensions since the binder needs to come out from the core of the part, in this way there are some rules that must be followed when designing a metal injected molding component:

- Avoid components where the major thickness is more than 12,5 mm,
- Avoid components with a mass over 100g (usually MIM parts are in the range of some tens of grams),
- Design a draft to help the ejection of the molded component;
- Avoid thickness of the wall less than 0,1 mm (otherwise there is a poor filling during the injection or the metal powder can plug), and the wall thickness should be as much uniform as possible.
- Design support part for the component to avoid deformation during sintering.

These limitations makes MIM the perfect technique for shaping small components with a complex geometry.

1.1 The MIM process

The MIM process is based on different steps that can be schematized as follows and as represented in figure 2:

- production of the metal powder;
- mixing with the polymeric binder to obtain the feedstock;
- injection molding to produce the green part;

- debinding;
- sintering;
- secondary operations.

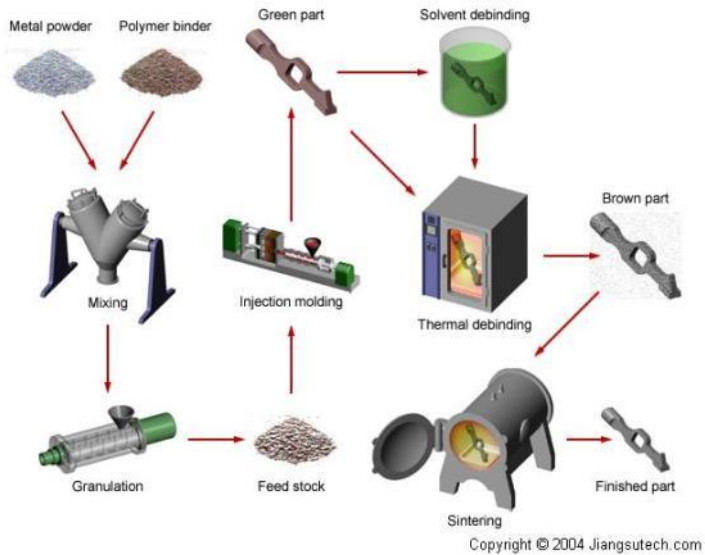


Figure 2: scheme of the MIM process 3].

Every single step has its own peculiarities, and the choices that can be made to complete each step give a lot of possibilities and bring to different results. In this way the final result is a tailored path through all the process. Sintering and secondary operations are similar to the processes used in the classic press and sinter technique. Sintering temperature is usually much higher for the MIM parts respect to press and sinter components. The union of the

high temperature and the fine powders used for the feedstock production, permits to reach densities up to 98%. In this way the mechanical properties of MIM parts are extremely high and near to the mechanical properties reached from the cast alloy with the same composition.

1.1.1 Powders used in the MIM process

The raw materials used for the production of the MIM feedstock are extremely important. The metal powder is of course the main point on which is important to focus the attention. The choice of the powder is fundamental on different aspects such as the brown strength, the shrinkage during sintering, the shape retention, the densification and final porosity, the mechanical properties at the sintered state and the heat treatability. A lot of metal and alloy powders can be used in the MIM process, they can be supplied with enough small size to start the sintering in the range of temperature where the binder is going to be decomposed [4]. This is extremely important because the binder is an organic compound and if it is trapped in the porosity during sintering the final alloy can be enriched in carbon with detrimental effects on the microstructure and mechanical and corrosion properties. Magnesium and aluminium are not widespread used in the MIM industry since the elevated oxidation of the surface of powders limits sintering, anyway many other metals can be used as : low alloy steels,

stainless steel, copper and copper alloys, titanium alloys, tool steels, cemented carbide and refractory metals.

The processes of powder production most used for MIM are the gas and water atomization and the carbonyl process. In all these cases the most important characteristics of the powder are size and shape; a very fine powder is required and the shape must be as rounder as possible to maximize the packing density and the solid loading of the feedstock. A spherical powder is preferable since it minimizes the anisotropy of shrinkage during sintering and the shape retention from the green part to the sintered part is improved. Figure 3 shows the typical distribution curve for a MIM powder and the relative roundness as a value that goes from 0 to 1 in case of perfectly spherical particles.

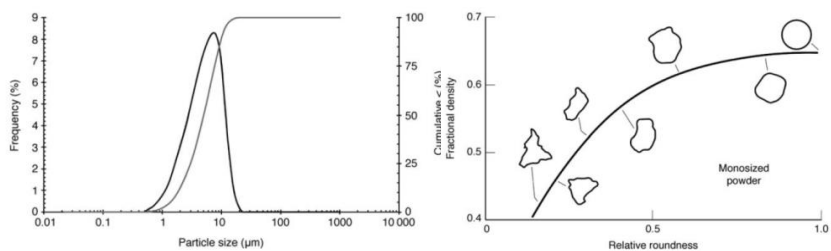


Figure 3. Typical MIM powder particle size distribution and the effect of the relative roundness on the packing density [1].

Another reason for this peculiar particles distribution and elevate roundness is the rheological behavior of the feedstock. The

presence of the metal powder as a load into the polymeric binder must not affect too much the moldability of the feedstock. But also on the metallurgical point of view a fine powder is important. The MIM process is totally different from the press and sinter regarding the shaping of the green part. The powder particles in the press and sinter process are plastically deformed in order to have a mechanical joining. The green strength, in this case, depends from this interaction and the green parts can be handled; with the sintering the final mechanical properties are reached. In the MIM process the powder particles are not plastically deformed and the green strength is due only to the presence of the binder. During the debinding process the binder is extracted from the green part and the strength is limited to very low forces between the particles. A fine powder can bring to a better green strength and gives a higher driving force in the first stage of sintering. In the most common cases the metal powder represents more or less the 60% in volume of the feedstock. So, when the binder is removed, the porosity of the green part is extremely high and it's necessary to have a large surface area of the particles to supply the driving force for the densification. That's way in common industrial MIM the powders come from a limited numbers of production processes. The plastic deformation in the press and sinter process is also a limitation. The yield stress should not be too high otherwise is impossible to obtain

a correct green density with a force that is not detrimental for the compaction tools. Because of this, prealloy powders cannot be used since the solution hardening due to the alloying elements increases too much the yield stress. In MIM this limitation does not exist, so also gas or water atomized prealloy powders can be used. This is important for the final chemical and microstructural homogeneity. So the characteristic of a good powder for the MIM process should be:

- A powder free from agglomeration but able to have enough interparticle friction to maintain the shape after debinding;
- Spherical or as much rounded as possible with a dimension up to 30 microns;
- Free from internal porosity;
- Good wettability by the binder.
- Not hazardous or explosive (violent oxidation can occur handling fine powders)

Table 1 summarizes the characteristics of the powders produced with the three processes mentioned above and figure 4 shows examples of typical MIM powders.

Powder production process	Size suitable for MIM	Shape	Materials	Cost
---------------------------	-----------------------	-------	-----------	------

Gas atomization	From 5 μm up to 40	Spherical	Metals and alloys	High
Water atomization	From 6 μm up to 40	Rounded	Metals and alloys	Moderate
Carbonyl	From 0,2 μm to 10	Spherical	Metals (commonly Fe)	Moderate

Table 1 : Typical characteristic of powder based on the production process. [5]

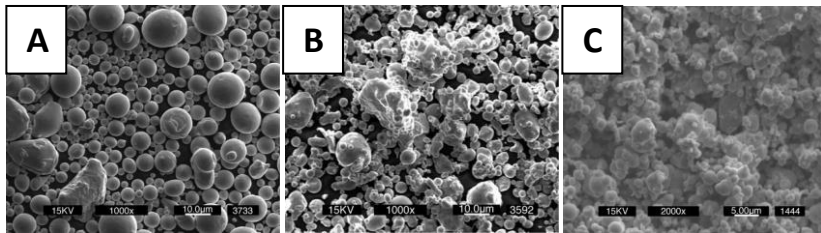


Figure 4. Three powders produced with different method: gas atomization (A), water atomization (B) and carbonyl process (C).

In MIM it's possible to adopt different alloying methods to reach the same final alloy composition [6,7]. Each route has its own advantages and the choice depends on the necessities of the produced part in terms of dimensional variations, geometry retention, chemical homogeneity and requested final density. It's possible to identify three alloying methods:

- **Elemental method:** This method is based on the adoption of elemental powders used in the correct ratio to reach the desired chemical composition. This powders are usually produced with the gas atomization method or in case of

iron and nickel with the carbonyl process. The chromium powder is produced by grinding the semi-product of an electrolytic process. For stainless steels, for example, the blended elemental route can be made by using carbonyl iron added with carbonyl nickel and electrolytic chromium. The control of the particle size distribution from lot to lot is an important issue that must be control. The adoption of this alloying methods is advantageous for the sintering behavior relatively to two characteristics of the powders and of the mix. First of all the use of carbonyl powder of extremely fine diameter gives a very high surface energy for sintering, and also the large chemical gradient related to the heterogeneity of the alloying elements is an added potential for the diffusion in the first stage of sintering. Neck growth in this condition starts at lower temperature and it's possible to reach a higher final density.

- Prealloy method: in this method every single powder particle has the same chemical composition of the final alloy. In this case powders are produced with the water or gas atomization process. The particle size distribution is usually larger in diameter. Therefore sintering start is delayed respect to the other alloying methods and the final density that can be reached is lower. The advantage is that

the chemical composition at the end of the sintering is perfectly homogeneous and this can be a positive aspect for having a uniform microstructure and a better hardenability.

- Master alloy: in this method the mix of powders is composed of an elemental powder added with a certain quantity of a water or gas atomized powder with an enrichment of the alloying elements needed. Of course the quantity of the enriched powder should balance the elemental one to reach the stoichiometry of the final desired alloy. The master alloy route is the preferred in the MIM process since the geometry retention is optimal, the final density at the end of sintering is elevated and the chemical homogeneity is very good.

1.1.2 Binders for the MIM feedstock

The binder is the medium that holds the metal powder particles during the injection molding and in the green state. The choice of the binder is , as for the powder, a fundamental issue in the feedstock development for the successful production of the component [8]. The binder characteristics determine the rheological behavior of the feedstock, its moldability, the green strength and the debinding process. The main characteristics of a good binder are listed in figure 5 :

	Desirable characteristic
Powder interaction	Low contact angle Good adhesion with powder Capillary attraction of particles Chemically passive with respect to powder
Flow characteristics	Low viscosity at the molding temperature Low viscosity change during molding Increase in viscosity on cooling Small molecule to fit between particles
Debinding	Degradation temperature above molding and mixing temperatures Multiple components with progressive decomposition Temperatures and variable properties Low residual carbon content after burnout Non-corrosive and non-toxic burnout products
Manufacturing	Easily available and inexpensive Long shelf life Safe and environmentally acceptable Not degraded due to cyclic heating High strength and stiffness Low thermal expansion coefficient Soluble in common solvents High lubricity Short chain length and no orientation

Figure 5. Ideal MIM binder characteristics [1] .

Usually the binder is not just a single polymer but a mix with accurate and specific quantity and characteristic of each components. Typically a binder consists of a principal component added with different additives with the role of dispersant agents, plasticizers or stabilizers. The most used binders can be divided in three categories.

- The thermoplastic binders that use a mixture of thermoplastic polymers [9]. The debinding process for these feedstocks is divided in two steps. The first step takes place

in solvent (water or organic); the largest part of the binder is removed and a continuous porosity is created through the volume of the green part. The second stage is the thermal debinding. The binder is composed in minimum part by a polymer that is called backbone polymer [10]. This should not be soluble during the first step and must retain the powder since the beginning of the sintering. That's way the decomposition of this polymer is a thermal decomposition during the heating of the parts in the furnace.

- The gellation binders are based on an hydration process that starts with the formation of a single molecule that during the process extends to the entire volume of the binder. This process is based on the use of water that is trapped within the structure. At the end of the gelation process the molecule formed retains the powders because of the extreme high viscosity achieved. The debinding process can take place by evaporation and by thermal process.
- The catalytic binders that uses a polyacetal binder based on polyoxymethylene. It's a proprietary technology [11]. The debinding is very fast but it's necessary to use nitric acid at

vapor state. The handling of this hazardous acid is one of the limiting factors of this technique.

In all the three cases it's extremely important that debinding does not damage the structure of the material. The decomposition of the binder is tailored to take place within a certain range of temperature, so that the gas produced by decomposition do not remain entrapped in the green part where they will evolve as defects in the sintered component. One of the most widely used binder is the thermoplastic one. In this case the larger volume of the binder is extracted in water added with a corrosion inhibitor. The backbone polymer is thermally decomposed.

1.1.3 Injection molding

Figure 6 represents a typical injection molding machine. The main parts are the injection unit and the clamping unit where the mold is mounted [12]

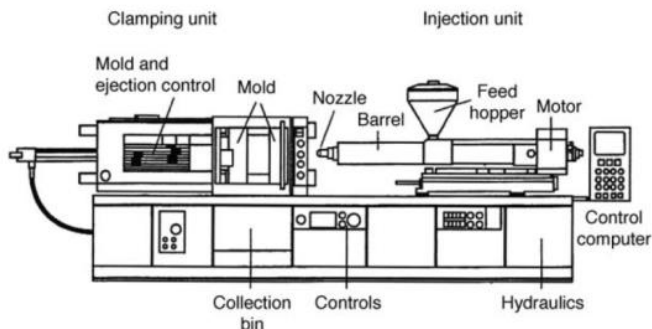




Figure 6. A schematic drawing of an injection molding machine[12] and an Arburg Allrounder injection molding machine.

The main characteristic for choosing an injection molding machine is the clamping force. Based on the clamping force is the area of the molded part and so its volume and weight. The molten feedstock is pressurized inside the tooling and the applied pressure opens the mold. The bigger is the part to be molded or the higher is the pressure the higher should be the clamping force available. That's way usually the clamping force is hydraulically supplied by an oil pump. Generally in MIM the volume of the molded parts is limited therefore the clamping force is not too high. In this case the clamping force can be supplied by an electric engine and the maintenance and operating costs are lower. The injection unit is the section where the feedstock is molten and pressurized to be injected in the mold. The unit is simply composed by a heated barrel and a screw to compress and shot the molten feedstock in the mold. In figure 7 a screw for the injection molding of plastic is shown.

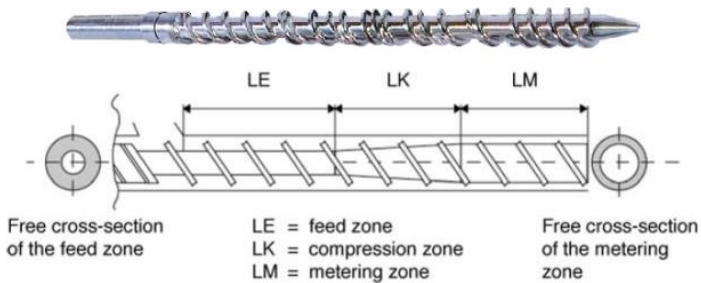


Figure 7. A screw for injection molding of plastic material with the different zones.

The granules of feedstock are fed into the barrel from the feed zone of the screw. The barrel is heated and the friction of the feedstock given by the torque applied by the screw in the compression zone helps the binder to reach the correct working temperature. The temperature should be high enough to avoid the freezing of the feedstock in the mold but it should not exceed the level at which the polymers in the binder can be deteriorated. The presence of the metal powder load in the feedstock helps to reach a uniform temperature faster. In the metering zone a final stirring of the feedstock is made to reach the best homogeneity. The injection is made as in the classic injection molding of polymers by a forward movement of the screw.

The injection molding machines used in MIM are not so different from those used for the injection molding of polymers. Of course it's necessary to consider that the polymer has a metal particles load.

Friction and the wear of the moving parts are higher. Therefore it's necessary to use special tooling with a better resistance to friction and wear but in some cases, in industrial practical work, some machine are used for MIM with no modification.

Another important issue is related to the geometry and design of MIM parts. The basic concepts behind the design of MIM components are the same of polymer injected parts. During sintering the dimensions of the molded part can shrink up to 15%, so the mold cavity must be designed considering this dimensional change. A particular attention is necessary to limit the thickness of the parts since the debinding time might result too long or, alternatively, defects might result from gas entrapment.

Figure 8 shows some design expedient that must be used in MIM.

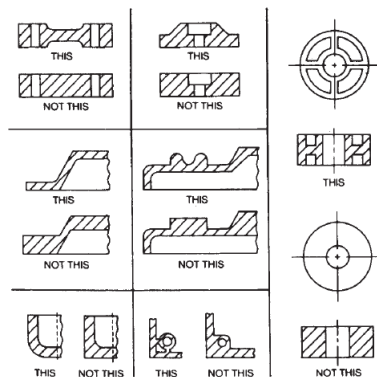


Figure 8. Specific design for MIM parts.

1.1.4 Debinding

In most cases feedstocks contain a primary and a secondary binder. The volume occupied by the binder is large, up to 45%. So, during debinding a very high volume of gas is produced by its decomposition. If the binder would be made of a single component decomposing in a small range of temperature, the part might either fail due to the pressure exerted by the gas, or contain surface bubbles. It's necessary to avoid this situation and the easier way to do it is to mix polymers with different decomposition temperatures or different way of debinding. The first binders for MIM were based on waxes. The mixture of waxes was made in order to have a very large temperature range of decomposition. The technique is valid but the problem is that the process is very slow especially if the component is thick. Nowadays the MIM industry is moving toward two direction regarding debinding, the water soluble binders and the catalytic (Catamold®) system. Both these systems require a primary and a secondary debinding.

Water soluble binder

The water soluble binder system is widely used in Europe and in Italy. The main constituent of the binder is polyethylene glycol (PEG) with low molecular mass [13,14]. This polymer is water soluble and the limited molecular mass is useful to make the molecules dissolve faster in water. The debinding bath is simply a chamber filled with

water and a corrosion inhibitor, if necessary, thermoset at around 50°C. The PEG dissolution takes some hours depending on the thickness of the part and at the end of the process the entire volume of the part contains an open porosity. This porosity is necessary for the secondary debinding. The secondary debinding is made thermally.. Usually this step is not made in the same furnace where sintering takes place but in a simpler one. The temperature reaches 600°C (700°C in the case of a presintering) in a controlled atmosphere. The polymer that is decomposed can be burned outside or collected in filters that must be cleaned after every batch.

Catamold® binder

Catamold® is a technology by BASF. In this case the binder is produced by mixing a major ingredients, the polyoxymethylene (POM) and a polyethylene. The primary debinding uses 4% of nitric acid at vapor state to convert the POM into formaldehyde in a range of temperature between 100°C and 140°C. There are some hazards related with the use of this binder. First of all the danger of using the nitric acid and then the formaldehyde formation. Formaldehyde is toxic and is explosive if reacts with oxygen; to avoid this problem the furnaces use a flux of nitrogen to take away the formaldehyde formed during the process that is burned in a chimney on the top of the furnace. At the end of the first debinding just the skeleton of

polyethylene remains to maintain the particles in place. The secondary debinding is made in the same way as for water soluble binders.

1.1.5 Sintering

Sintering is the main step of the process if no secondary operations as heat treatments are required. Sintering promotes the formation and growth of necks between the particles by mass transportation mechanisms [1]. The driving force is the excess of Gibbs free energy related to the surface of the particles.

In MIM the particles size is extremely low respect to the classic PM techniques. The total specific surface area of the particles is very high and the sintering kinetics is, at the beginning, accelerated vigorously by this [4]. That's one reason why MIM parts reach a very high density. The typical explanation of the sintering is based on the two spheres model. Two spheres with equal diameter touch each other in one single point, and with the increase of temperature mass transport mechanisms work to minimize the total free energy , by creating a neck between the particles. With time passing the neck grows and the last theoretical step is the formation of a single sphere to have the least free energy possible for the system.

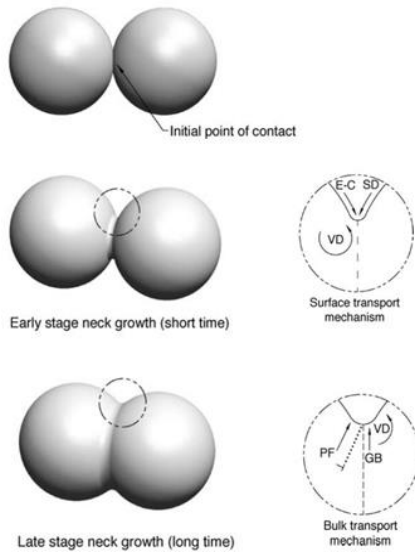


Figure 9. The evolution of the particles during sintering.

The mass transport mechanisms involved in sintering can be divided in some individual mechanism:

- *Evaporation and condensation* : materials characterized by high vapor pressure under high temperatures can react with the sintering atmosphere and form a volatile species that can subsequently condense on the neck in order to reduce the total surface. For metallic system the contribution on sintering of this mechanism is negligible.

- *Surface diffusion*: this mechanism is based on the migration of the defects present on the surface of the particle. At the first stage of sintering this is the preferential mechanism by which the neck is formed. It has an activation energy lower than the bulk diffusion so at lower temperature the surface diffusion is prevalent.
- *Volume diffusion*: this mechanism is due to the diffusion of atoms through defects, for example dislocations and vacancies inside the grains of a crystalline material as a metal. This mechanism is basic for the neck formation stage but especially for the densification through the neck growth.
- *Grain boundary diffusion*: the activation energy of this mechanism is lower than the one required for the volume diffusion so the grain boundary diffusion is active before the start of the volume diffusion. It uses the great quantity of defects present on the grain boundaries that become the highways for the diffusion of atoms.

From a more practical point of view sintering of MIM parts is made in batch or continuous furnaces. In most of the cases sintering processes for MIM are made in batch furnaces. The continuous furnaces are more common in the classic press and sinter technique since MIM requires higher temperatures respect to press and sinter

and the continuous furnaces that can reach this high temperature are extremely expensive. Another reason why batch furnaces are used deals with materials. MIM is used massively to produce stainless steel and titanium alloy parts that require either vacuum or highly controlled gas. Only in batch furnaces the right sintering conditions for these alloys can be obtained. The atmospheres used are different but in all cases are protective or even reducing: N_2 , Ar , H_2 or mix of these gases, but also vacuum (figure 10).



Figure 10. A vacuum furnace for sintering MIM parts.

1.2 Two-materials injection moulding

In the future of MIM a very important issue is the development of the two component injection molding. By this technique it's possible to couple in the same part two different materials, either two metals or metal and ceramic, to produce a composite with a specific combination of properties. This technology is used since many years

ago in the field of injection molding of plastics to produce parts with two different polymers or two different colors. In many cases engineers require different mechanical or technological properties in the same product, for example different corrosion behavior, different hardness or magnetic behavior. The 2C-MIM can be the answer to this requirement, a fast and feasible route to couple two materials in one shot . Feedstocks that can be used in this process are the same as for the classic MIM, the required rheological behavior of the feedstocks is similar, the difference is evident during the molding of the component. As for the polymers there are two ways to mold a piece made by two different feedstocks : the co-injection molding and the over-molding[1].

- In the over-molding the injection machine is equipped with two screws that can melt two different feedstocks and the mold is made of two different cavities. The first step is filling the first cavity (that is the smaller one) with the first feedstock. Subsequently there is a mold rotation and the molded part is inserted in the second cavity where there is the real over-molding made using the second feedstock. In many cases the machine is equipped with one only screw so it's possible to have one single feedstock to be injected. The operation can be made manually. The part is moulded using one mold with the required geometry and then ejected and

stocked until room temperature. After having equipped the injection machine with the second mold and the second feedstock, the previous molded part is inserted in the cavity and the free space is filled by the injection of the second feedstock. This manual process is more time expensive but is cheaper in term of equipment since it's not necessary to have a double screw injection machine or a tooling that can rotate the mold. At the end the part is ejected and processed in the same way as a classic MIM part with some consideration that must be taken in account to avoid cracks.

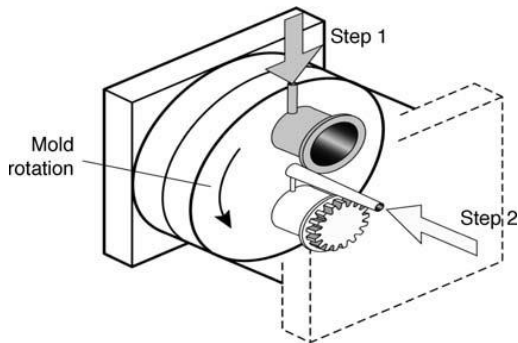


Figure 11. The scheme for an over-molding process of 2C-MIM components [1].

- The co-injection molding is a more complex process. It's widely used in the injection molding of polymers. The purpose is to create a part with a core made of a different

polymer respect to the skin. The machine used for injecting is equipped with one, two or three channel system and two screws where the two feedstocks are molten. In the single channel system the first feedstock is injected and subsequently the second one is injected too. The first one is then expanded by the pressurized second molten feedstock and adheres to the cooled mold surfaces forming a skin, the second one is filling the core of the component. In the multichannel system the two feedstock can be injected at the same time. Figure 12 represents the technique adopted for the co-injection molding of plastic feedstocks.

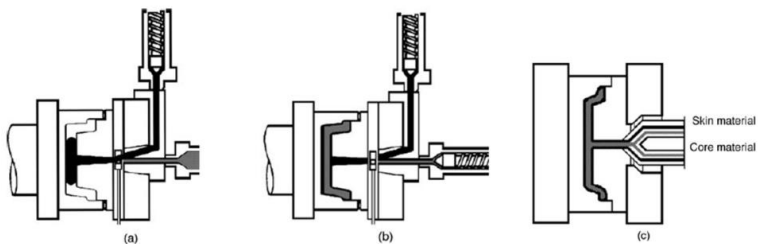


Figure 12. Scheme of the co-injection molding by one (a), two (b) and three (c) channel machine [1].

The 2C-MIM can be ideally divided in two steps: co-injection and co-sintering. The choice of the feedstock is very important for a good result during both the two steps. The behavior during the debinding of the polymer must be very similar between the two feedstocks,

that must have the same binder composition and debinding method. As far sintering is concerned, a too large difference of the shrinkage can lead to crack formation that will remain as a defect in the sintered part. The control of the powders dimension and the chemical composition is extremely important to avoid defects and to produce a strong interface between the two alloys. After debinding the resistance of the brown part is given just by the friction between the powder particle and it's typically in the order of 1MPa [1]. Even the difference in the thermal expansion could be detrimental for the powder cohesion. This is the most difficult moment for the survey of the part but also the first part of sintering is extremely important. At the beginning of the sintering the porosity in the structure can be up to 45% in volume. This porosity acts as a defect itself, with the increase of the temperature also the plasticity of the metal increases. So in the first part of the sintering the shrinkage of the two powders should be as much similar as possible to avoid the breakage of the component or defects as delamination or crack formation between the two powders. In the second stage of sintering, when the temperature increases and during isothermal holding at high temperature the plasticity of the material is high enough and higher differences between the shrinkage of the two powders can be tolerated.

The difficulties to manufacture a no defect 2C-MIM part are very high. Till nowadays only prototypes were produced and no mass production of two metal component were started. In any case the potentiality of this technology is very high and the elevated complexity of shapes and properties requested by many mass productions will push this technology to an industrial production in the future.

Bibliography

2.0 2C-mim. Scientific context

Defect free co-injection and sintering of two different metals or alloys is not an easy result to obtain. The geometry of the part of the component for each feedstock is very important but a perfect matching between the sintering behaviors of the feedstocks is necessary. Simchi et al. proposed in 2005 an approach for assessment of the sintering behavior of co-injected feedstock for PIM based on the Apparent Co-Sintering Index (ACSI) [15]. The method considers certain values of temperature and shrinkage during the dilatometric test and using the correct equation is possible to calculate a specific value. The calculated value of the ACSI should be less than 15 to make a defect less component, the lower the ACSI is the easier is obtaining parts without defects. Since stainless steels represent more than the half of all global MIM

production, in developing 2C-MIM the attention is mainly focused on these alloys. Stainless steel atomized powders are supplied in different size distribution and alloying methods. In many papers in literature the alloys used are an austenitic and a ferritic steel. Many studies start from the dilatometry study of the dimensional changes during sintering and the evaluation of the mismatch between the two materials. Mulser et al. highlighted the idea that the mismatch between the feedstock can be divided in three types [18] As shown by figure 13 there can be a mismatch at the initial stage of sintering (A), the mismatch during the intermediate stage (B) and the mismatch in the final stage [A].

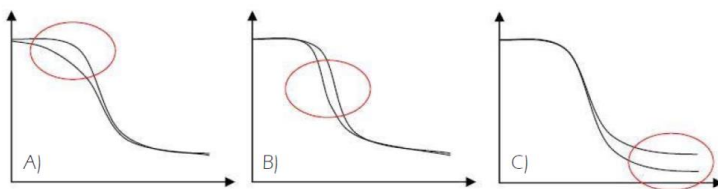


Figure 13. Types of mismatches that can be encountered during a co-sintering cycle[18].

In the same study dilatometry the mismatch between feedstocks of an austenitic and a ferritic stainless steel varying the particle size distribution of the powders was analyzed. It's well known that the effect of the particle size is extremely important to enhance shrinkage. On the other side it's necessary to consider the structure

of the two alloys. In the BCC structures the self diffusion of iron is higher and sintering can start earlier and faster respect to an FCC alloy [17]. This is an important reason for having large mismatch. The tendency is to avoid the mismatch in the initial stage of sintering at low temperature when the neck size is very small and the plasticity of the metal is still low.

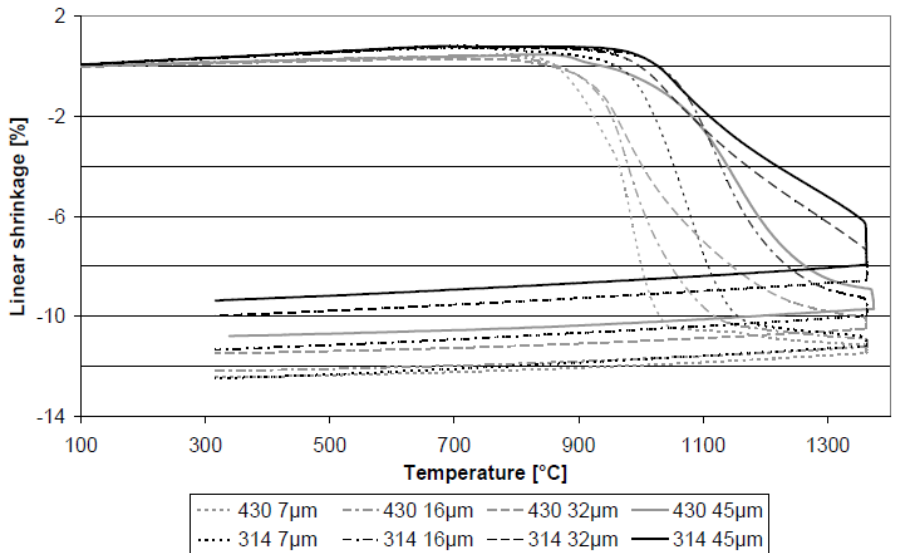


Figure 14. sintering cycles by Musler et al.

In figure 14 the result of the dilatometric sintering cycles of Musler et al. on the different feedstock is shown. Two conclusion can be highlighted. First of all as the particle size is decreased the shrinkage is anticipated and the final density is higher. This is valid for both

the austenitic and the ferritic stainless steels. On the other side the ferritic steels anticipates the sintering respect to the austenitic one. The more the dilatometry curves of the two feedstock are similar the more is possible to achieve a crack free interface. As the compositions between the two metals are different diffusion of elements is observed and the formation of an interface is widely demonstrated [A,C]. The diffusion of elements is limited to some hundreds of microns from the interface but it's deep enough to create a completely different microstructure. Whenever an austenitic and a ferritic stainless steel are coinjected with no cracks, the interface is characterized by the presence of austenite, martensite, and ferrite [18]. Far from the interface the microstructure that of the two base materials. As explained from Dutra et al. the characterization of the interface is a basic point. Different instruments can be used to do this, as reported in the table 2.

Technique	What can be detected?	Restrictions
Optical microscopic analysis	Cracks, phases, grain size, grain boundaries, etc.	Only a single slice of the sample is examined
EDX/SEM line scan	Chemical composition of base material and	Only linear measurements. Pores

	interdiffusion layer	may hide the results
Thermo-Calc/ DICTRA simulation	Chemical composition and interdiffusion profile	Thermodynamic equilibrium is assumed for simulation
Schaeffler diagram	Phases (Estimation)	Fast cooling is assumed, The chemical composition must be previously known.
Hardness profile	Mechanical properties and estimate phase formation	Phases with similar hardness are not distinguished
Tensile test/ fractured surface	Mechanical properties	Limited information about the interface
3D computational tomographic images	Cracks	-
X-ray Analysis	Phases	-
Electron microscopy analysis	Grain size, grain boundaries with higher magnitude respect to the optical microscope	-

Table 2. Techniques for the characterization of the interface produced by co-sintering[16].

The presence of the interface is related to the interdiffusion of elements so the most important analysis to be done is the EDXS line

scan. In this case it's possible to analyze the concentration profiles of the elements from the interface to the base material. As explained in the table these data can also be used to evaluate the possible phase formed during cooling. For example (figure 15) the crossing between the content of elements and the Schaeffler diagram can reveal the presence of martensite in the case of co-sintering of an austenitic and a martensitic stainless steel.

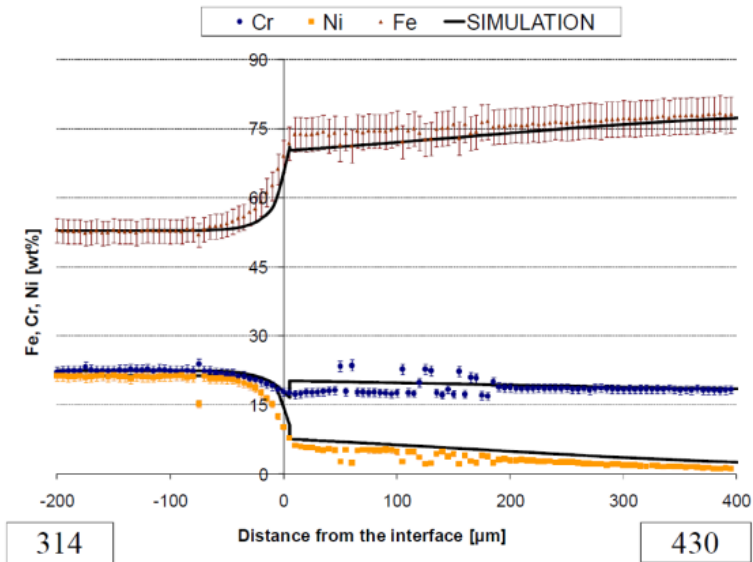


Figure 15. Crossing between the Dictra simulation and the EDXS analysis[16].

3.0 Experimental procedures

3.1 Sample production

All the samples were produced at MIMest S.p.a. in Pergine Valsugana. The feedstock used is supplied by commercial partners with the requested powder characteristics. The powder composition as declared by the supplier is reported in table 3. For each steel, two types of feedstocks were used based on both prealloyed and master-alloyed powders.

	Cr [%]	Ni [%]	Mo [%]	Mn [%]	Si [%]	C [%]	Fe [%]
430	16,9	-	-	0,58	0,44	0,09	balance
316L	17,5	12,8	2,1	0,12	0,32	0,01	balance

Table 3 : compositions of the feedstocks as declared by the supplier.

Samples are produced in two steps. The first step is the molding of the external 430 ring. The molding machine is an Arburg Allrounder 570. The molding conditions are : 190°C the temperature of the feedstock and 1100 bar the injection pressure. After the molding the samples are stocked waiting for the second feedstock injection. After the mold substitution, the 430 molded parts are heated to 70°C to improve the adhesion between the binders and avoid the second feedstock to freeze on the surface of the solid 430 feedstock before the complete filling of the cavity. The second molding is

made with the same condition as the first one. In figure 16 the geometries of the two injected parts are visible.

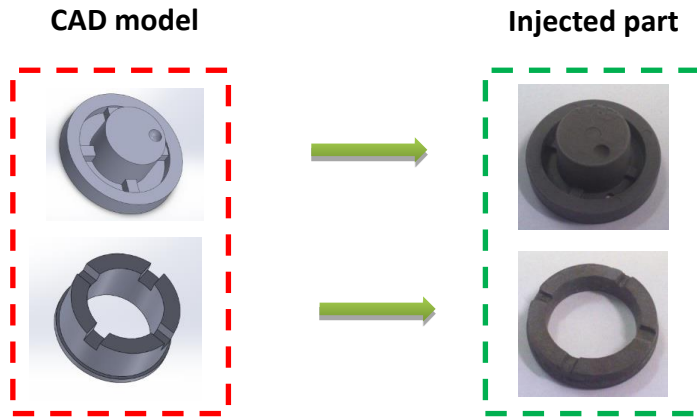


Figure 16: the cad model of the two parts and the effective co-injected part.

The subsequent step is the debinding. The debinding is also divided in two steps, the first one is the water debinding. The co-injected parts are immersed in a thermostable bath of water added with a corrosion inhibitor, the debinding rate is 4mm/h. The parts are then disposed on alumina plates and inserted into a furnace for the second stage of debinding, the thermal debinding. Here the green parts are heated up to 600°C, a temperature 100°C higher than the one necessary for the decomposition of the backbone polymer. The purpose in this case is also to obtain an initial sintering state that increases the strength of the brown parts that must be moved into

another furnace, a TAV MIM vacuum furnaces with metal chamber (Molybdenum) suitable for sintering of stainless steels, titanium, ceramics, etc., avoiding the formation of cracks. In the second furnace the complete sintering takes place. The atmosphere used is 100% H₂. The heating rate is very low (2°C/min) to maintain as much as possible the temperature homogeneity all over the volume of the chamber and to avoid too high gradients of temperature within the single parts. The sintering temperature was 1300°C, commonly used for the sintering of MIM stainless steels. The cycle used for the different lots of sintered parts are different only from the isothermal time at the sintering temperature. The isothermal steps were 0h and 1h at the beginning, and successively other two cycles with 20 and 40 minutes isothermal holding. The cooling is made in the furnace with the maximum cooling rate allowed.

3.2 Metallographic preparation and analysis

The first step was a visual observation of the external surface looking for evident cracks. If there were no cracks the metallographic specimens were prepared. Samples were mounted using phenolic resin and a Struers Labo-press 3 hot mounting machine. The surface visible after mounting is the bottom part of the specimen. To reach the depth at which the two steel rings are visible it was necessary to grind a certain thickness of the 430 ring as shown in figure 17.

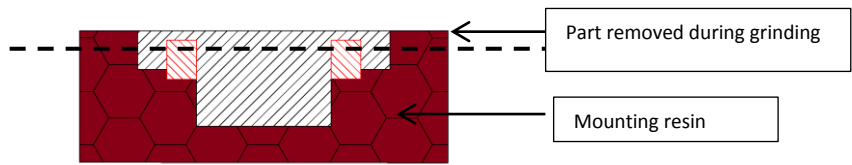


Figure 17. Mounted sample section.

This was the first step during the grinding of the sample surface. The papers used for grinding are silicon carbide papers with size of 220, 500, 800 and 1200 water lubricated. For polishing diamond pastes of 3 microns and 1 microns were used. The microhardness tests were carried out with a 0,1 N weight using a Leitz Micro Hardness Tester equipped with a digital camera and the software Alexasoft X-Vick for the automatic measurement of the microhardness. The metallographic etching was made with Vilella reagent (45ml of glycerin, 30 ml of HCl, 15 ml of HNO₃). The digital images were taken under an optical Zeiss Axiophot microscope. The main attention was focused directly on the co-injected specimen with the geometry of the final component. Tensile test specimens (MPIF Standard 50 “Preparing and Evaluating Metal Injection Molded (MIM) Sintered/Heat Treated Tension Test Specimens”, figure 18) were produced to investigate the mechanical resistance of the microstructural constituent produced by interdiffusion between the two steels at the interface between different powder particles

during sintering. Specimens were produced using a 50/50 (volume %) feedstock obtained by mixing the 316 and the 430 feedstocks. This way, the microstructural constituent produced by interdiffusion resulted predominant in the sintered specimens. Tensile specimens of the austenitic and the ferritic stainless steel were produced, too, for sake of comparison.

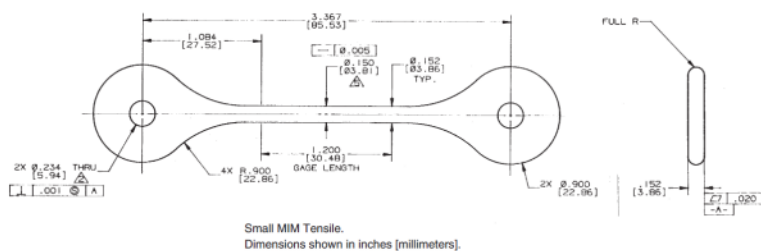


Figure 18. The MPIF design for the tensile test specimen for MIM.

Prismatic specimens were produced, too, by co-injecting the two feedstocks in order to obtain a flat interface.

3.3 Scanning Electron Microscope observation and EDXS analysis

A Philips XL 30 SEM equipped with a EDAX analysis was used (figure 19). The samples were prepared in the same way as for the light optical microscope observation followed by a conductive coating deposition. All the observations and analysis were performed in high vacuum to improve the precision of the measurements.

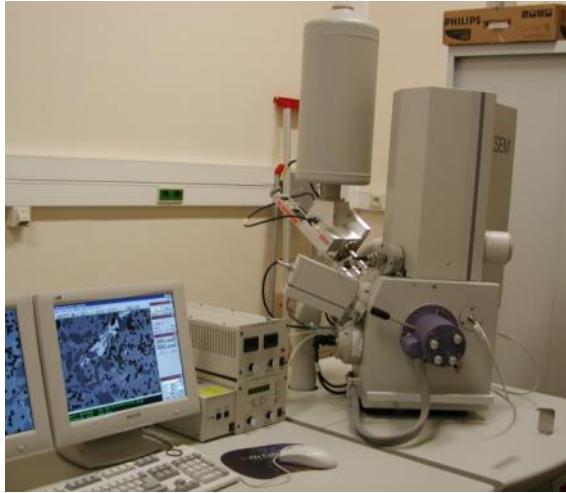


Figure 19. The Philips XL 30 electronic microscope.

3.4 Mechanical tests

Tensile tests were performed by an Instron 8851 servo hydraulic testing machine. The strain rate was 1mm/min. The elongation was calculated with an extensometer. . The raw data were then smoothed to delete the background noise due to the pressure system of the testing machine. The yield stress was calculated as the stress at 0,2% of permanent deformation. True stress and true strain were calculated as:

$$\sigma_T = \sigma (1 + e)$$

$$\varepsilon_T = \ln(1 + e)$$

The plastic deformation steps of the tensile curves were fitted using different strain hardening models reported in literature:

- Ludwig-Hollomon eq. (commonly used for most of the metals)

$$\sigma = K * \varepsilon^n$$

- Ludwik eq. (used for TRIP Steels)

$$\sigma = \sigma_0 + K * \varepsilon^n$$

- Stable austenite eq. (used for austenitic steels)

$$\sigma = K * \varepsilon^{(n_1 + n_2 * \ln(\varepsilon))}$$

3.5 Dilatometry test

The samples used for the dilatometry were cut from the tensile specimen. Rounded specimens 4x9 mm were obtained and tests were made using a Baher DIL 805, an induction heated dilatometer used in the heating ring hardware configuration. The gas atmosphere was static Ar added with 5% of H₂ as reducing agent. The temperature program is based on a heating rate of 2°C/min up to 1300°C, from this point the temperature increases of 1°C/min up to 1360°C. Figure 20 shows the chamber of the dilatometer.

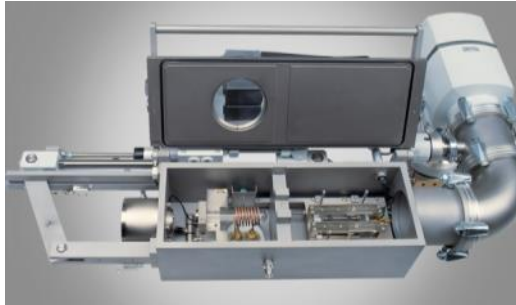


Figure 20. The Baher DIL 850 induction heated dilatometer.

The result of the dilatometry test were used for the calculation of the ACSI (Apparent Co-Sintering Index) of the for each combination of feedstocks [15]

Model Description

When two materials with dilatometric curves shown in figure 21 are subject to co-sintering, three temperatures are of great importance on the process:

(I) The start of sintering temperature (T_{start}), at which 0,5% shrinkage occurs during heating.

(II) The maximum shrinkage rate temperature (T_{max}), at which maximum shrinkage rate occurs.

(III) The sintering temperature (T_s), at which the specimen is sintered.

Three dimensional changes are defined:

(I) the expansion of the sample due to heating (α_{CTE}) that is related to the coefficient of thermal expansion.

(II) the shrinkage occurring at T_{max} (α_{max}).

(III) the amount of shrinkage (α_s) at T_s or after isothermal holding at T_s .

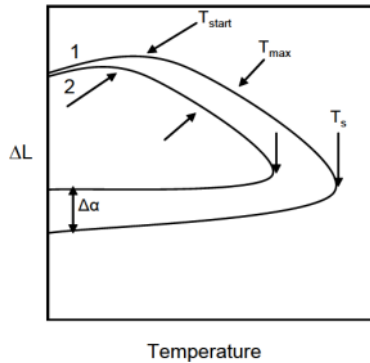


Figure 21. Typical dilatometry curves for PM parts.

The combined effect of these processing parameters is expressed by defining the following temperature and dimensional change functions:

$$f(T) = \left(\frac{T_{Max} + T_s}{T_m}\right)_2 - \left(\frac{T_{Max} + T_s}{T_m}\right)_1$$

$$f(\alpha) = (\alpha_{CTE} \cdot T_{start} + \alpha_s)_2 - (\alpha_{CTE} \cdot T_{start} + \alpha_s)_1$$

$$f(\alpha, T) = f(\alpha) + i f(T) \quad \text{where } i = \sqrt{-1}$$

The apparent co-sintering index (ACSI) is the mathematical length of the singular vector. The lower the ACSI value, the better compatibility of the two components. In the experiments that were successful in literature the minimum requirement for the ACSI number for co-sintering is $ACSI=15$. $ACSI=0$ is absolute or perfect compatibility and $ACSI>15$ is a sign of insufficient compatibility for co-sintering.

3.6 Corrosion tests

The specimens for the corrosion test were mounted using a cold Struers epoxy resin system. They were polished with 1 μm diamond clothe and the edges between the specimen and the resin were sealed with additional epoxy resin to avoid any crevice corrosion. The real area of each sample was measured. The machine used for the potential dynamic analysis is an EG&G Princeton Applied Research Potentiostat/Galvanostat Model 273A and PowerSuite software, the used solution was 0,5M of H_2SO_4 in water. The potential was continuously increased from -0,6 V to 1,6 V. The surfaces of the samples after the potentiostatic test were examined under the SEM microscope.

4.0 Results and discussion

The first experiments were made using a prealloyed powder for the two steels.

4.1 430 Prealloy – 316L Prealloy route

4.1.1 Powder analysis

430 prealloy

Figure 22 shows two SEM images of the prealloyed 430 powder.

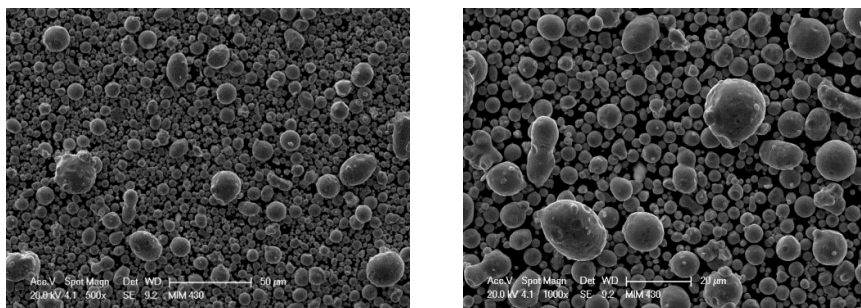


Figure 22. SEM images on the 430 prealloy powder particles.

The powder appears rounded and apparently follows a bimodal distribution. From the EDXS analysis it is evident that the chemical composition is the same for the fine and the coarse fractions of the powder, as shown in figures 23-25 where SEM images and EDXS spectra collected on particles with different sizes are shown.

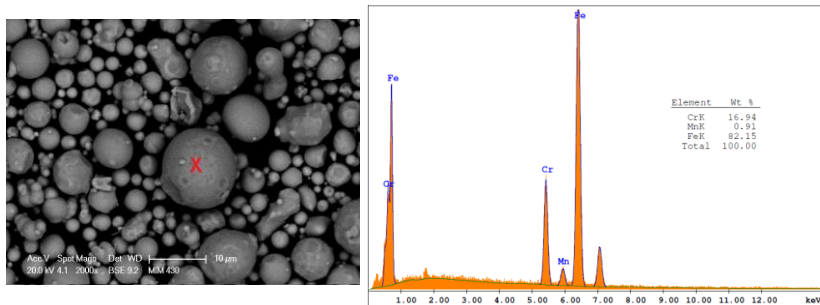


Figure 23. EDXS analysis on a 430 coarse particle.

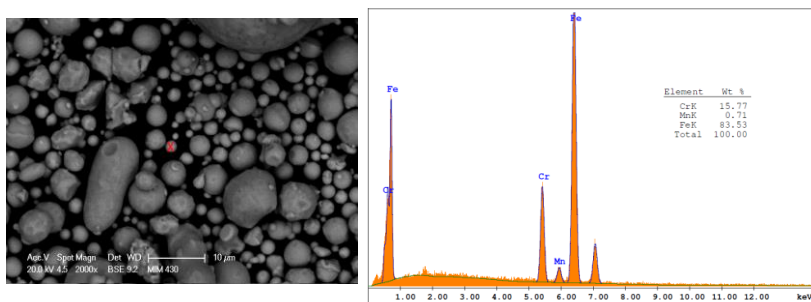


Figure 24. EDXS spot analysis on a very fine 430 particle.

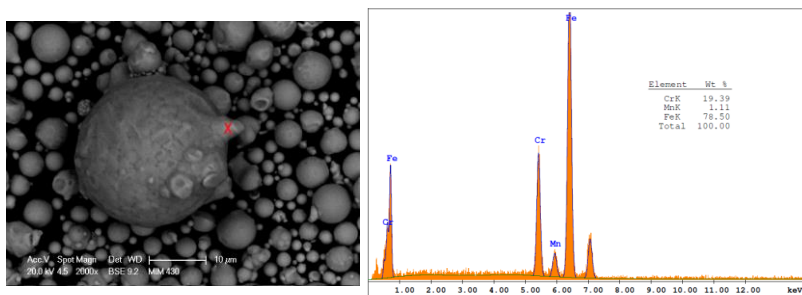


Figure 25. EDXS analysis on a satellite of a coarse 430 particle.

316L prealloy

Figure 26 shows two SEM images of the prealloyed 316L powder.

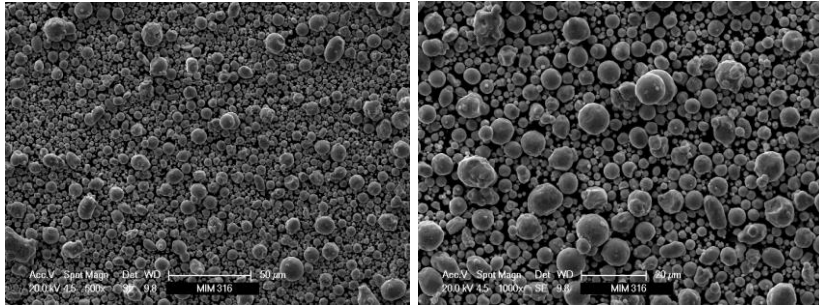


Figure 26. SEM images of the 316L prealloy powder particles.

Even in this case the chemical composition is the same for all the particles, irrespective to their size, as shown by the results of EDXS analyses shown in figures 27-29; analyses were carried out on the particles labeled in the relevant SEM analyses.

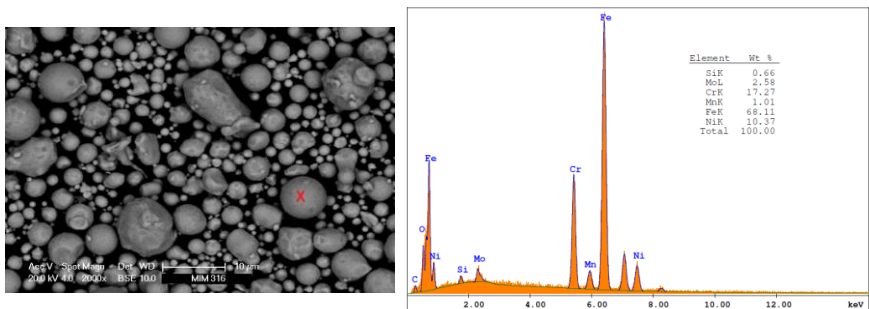


Figure 27. EDXS analysis on a 316L prealloy rounded particle.

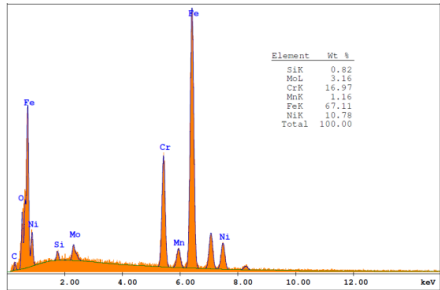
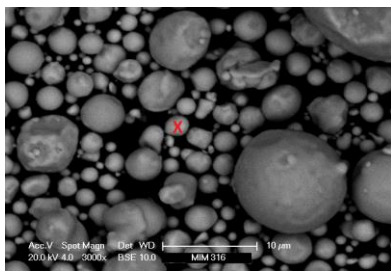


Figure 28. EDXS analysis on a 316L prealloy fine particle.

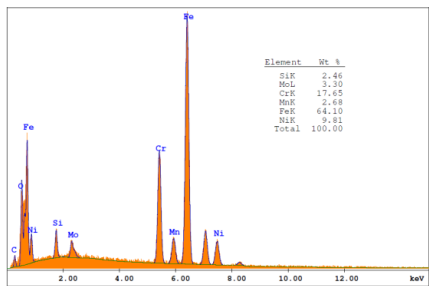
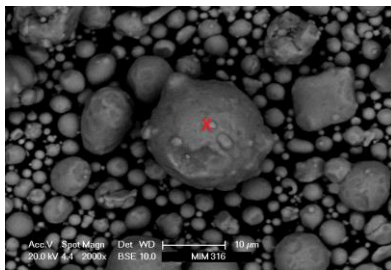


Figure 29. EDXS analysis on a 316L coarse particle

4.1.2 Dilatometry tests

Dilatometry tests were performed to evaluate the possible mismatch between the dimensional change of two feedstocks. Figure 30 shows the dilatometric record of the two green materials (after debinding) up to the isothermal sintering temperature of 1300°C.

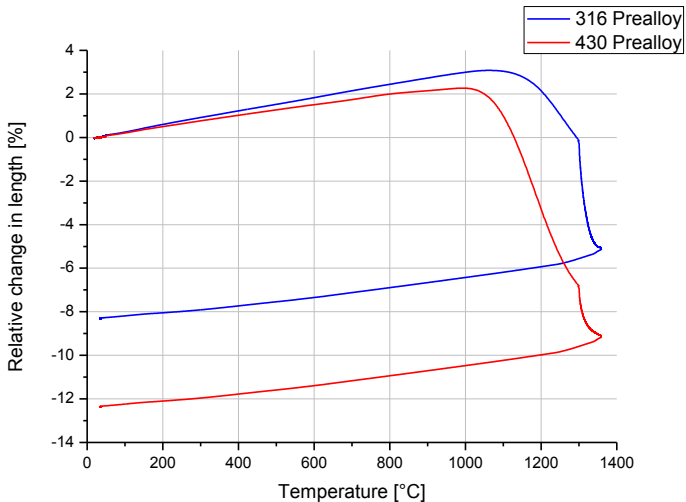


Figure 30. Plot of relative change in length of the dilatometry test on the two prealloy feedstocks.

The dilatometry test shows that during heating, before shrinkage starts, the two plots diverges, but this is not particularly problematic. The real mismatch is taking place at a temperature above 1000°C. This is extremely dangerous for the integrity of the

co-injected part since the strength of the material is still low in this stage. Sintering starts at different temperatures: 1060°C for the 430 and 1140°C for the 316L; this was expected because of the higher self-diffusion of iron in the bcc lattice of alpha phase than in the fcc one of the gamma phase. The final shrinkage for the two feedstocks is very different. Shrinkage rate is also very different, as shown by figure 31.

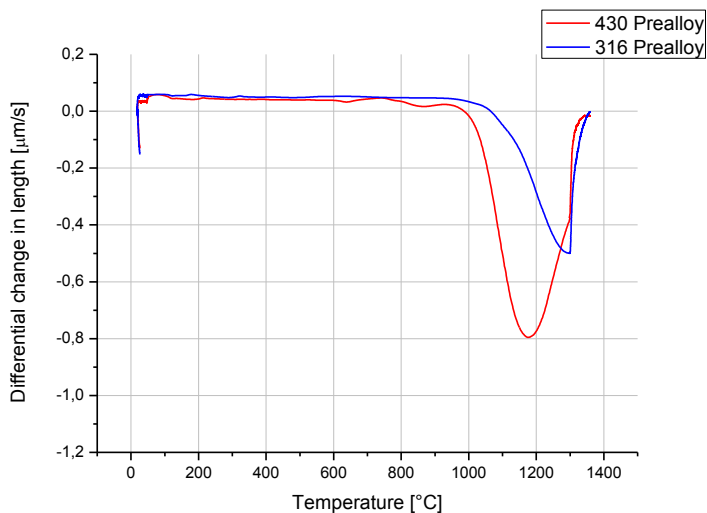


Figure 31. Plot of differential change in length of the dilatometry test on the two prealloy feedstocks.

The result of the dilatometry test evidences that these feedstocks are unsuitable for co-sintering since the different shrinkage behavior will give rise to delamination and/or cracks. To have a

confirmation of this, the equations explained in chapter 3.4 were used to calculate the maximum stress at the interface due to the dimensional change mismatch. The calculated stresses is reported in figure 32. It is very low until the temperature at which the mismatch between the dimensional change of the two materials occurs. Here the stress exceeds the maximum stress allowed, that corresponds to the yield stress of the two steels at about 1200°C in a condition of a poor sintering, that means quite a large porosity and weak interparticle bonding. Such a stress was estimated around 1-2 MPa. .

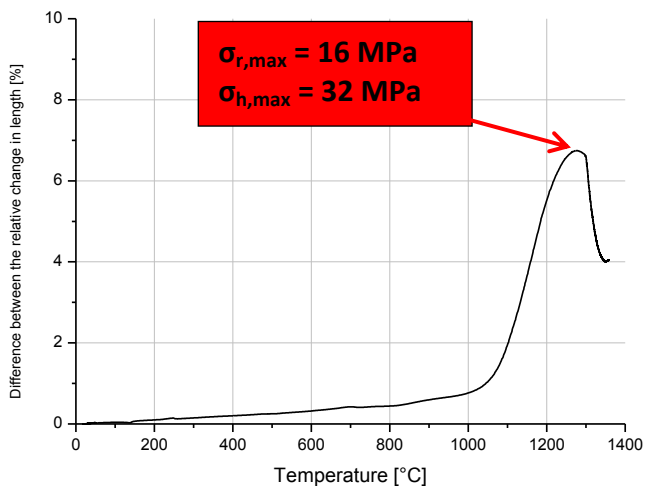


Figure 32. The calculated interface stress during the co-sintering cycle.

The result after the injection molding and sintering is coherent with the evidences highlighted by the dilatometric study. Cracks are present in the radial and also in the tangential direction, as clearly observed in figure 33..



Figure 33. The sintered component produced using the two prealloy feedstocks, evident tangential cracks and delamination are visible.

4.2 430 Prealloy – 316L Master Alloy route

From the previous experiment it came out the necessity to anticipate the start of sintering for the austenitic steel. The only way to do this is changing the powder typology. A master alloy powder can be the right solution. In this case the finer particle size and the heterogeneity of the chemical composition enhance shrinkage. The finer particle size increases the driving force linked to the surface energy, the chemical heterogeneity provides an additional contribution to driving force due to the mixing energy.

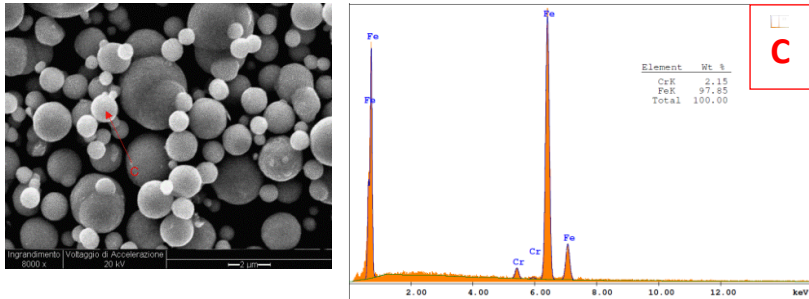


Figure 37. A spot on an iron particle.

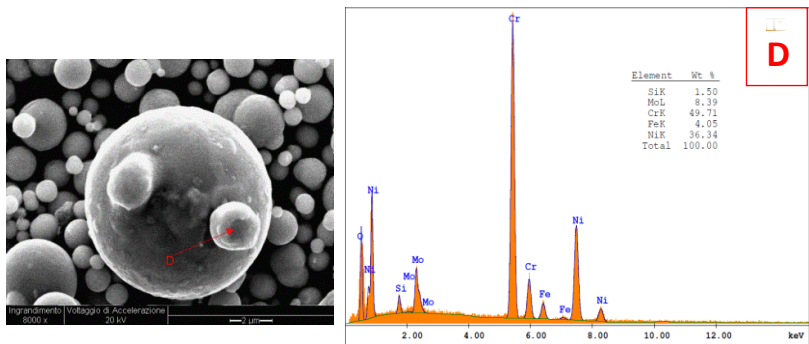


Figure 38. a spot on a satellite of a gas atomized particle.

The powder is composed by two fractions : a very fine carbonyl iron powder and a gas atomized master alloy with chromium, nickel and molybdenum as alloying elements in a ferrous matrix.

4.2.2 Dilatometry tests

In figure 38, the dilatometry records of the two green materials are reported, still up to an isothermal sintering temperature of 1300°C. In figure 39 the differential shrinkage curves are reported.

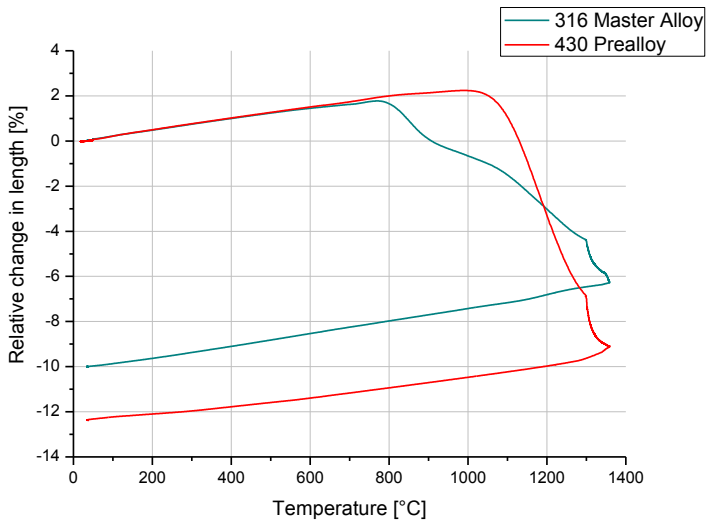


Figure 39. The relative change in length plot of the dilatometry test on the 430 prealloy and the 316L master alloy feedstocks.

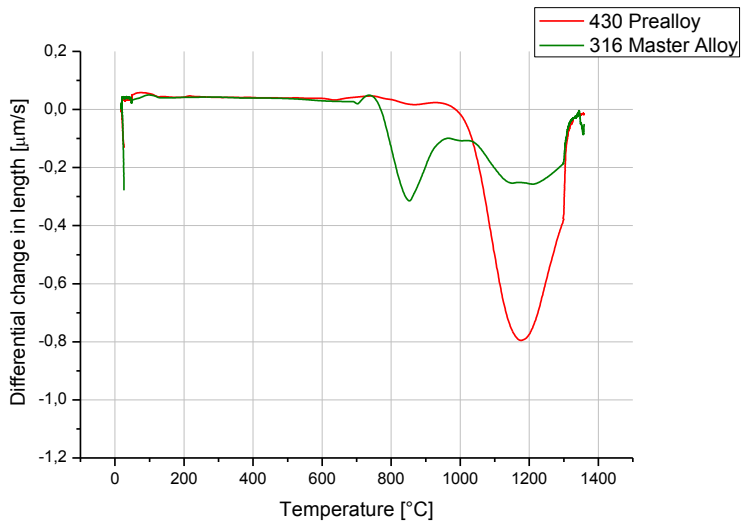


Figure 40. The differential change in length plot of the dilatometry test on the 430 prealloy and the 316L master alloy feedstocks.

Using the 316L master alloy, sintering shrinkage starts earlier (790°C). The desired effect has been reached but now it's the 430 prealloy that shrinks at a higher temperature respect to the 316. SEM analyses highlight an additional contribution to the enhancement of the shrinkage in 316L powder, due to the large fraction of carbonyl iron, with its bcc lattice where diffusivity is, as mentioned before, greater than in fcc lattice of austenite. Until diffusion of the alloying elements promote its transformation in austenite, such a large fraction of bcc iron gives rise to a large shrinkage that is not possible in the prealloyed fully austenitic

powder. Also for this case the maximum stress calculated exceeds the maximum stress allowed, as shown in figure 40, even if it is much lower respect to the complete prealloy route.

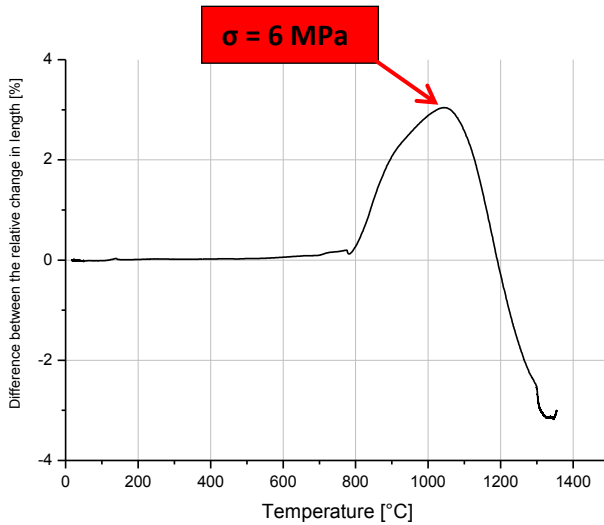


Figure 41. Calculated stress during the co-sintering.

Cracks may still be expected after sintering. They were not directly observed on the sintered parts, as in the previous case. However, after metallographic preparation, evident cracks were found all around the external perimeter of the austenitic ring, as shown in figure 41.

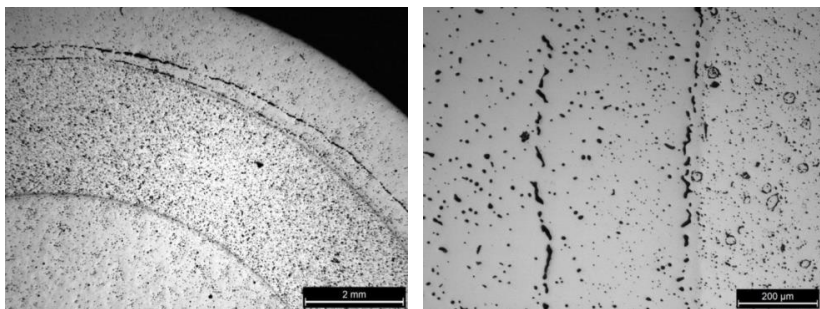


Figure 42. The cracks visible after polishing between the 430 and the 316L rings.

4.3 430 Master Alloy – 316L Master Alloy route

To reach a good balance between the two sintering kinetics, also the 430 was used in the master alloy configuration. The massive presence of carbonyl iron powder in both the feedstocks should balance the shrinkage kinetic during the first stage of sintering dramatically reducing the mismatch observed in the previous tests.

4.3.1 Powder analysis

430 Master Alloy

SEM images and the EDXS point analyses on some selected particles

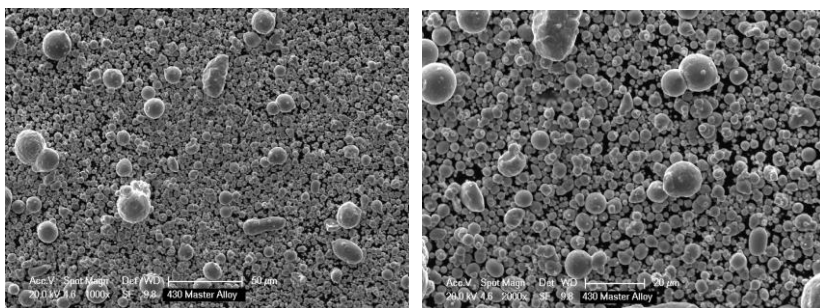
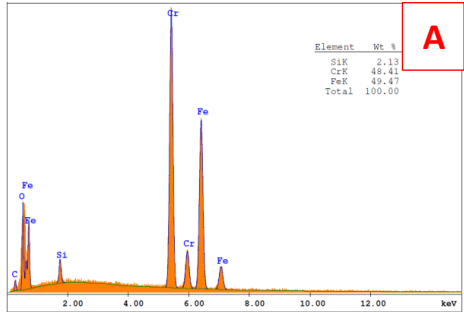
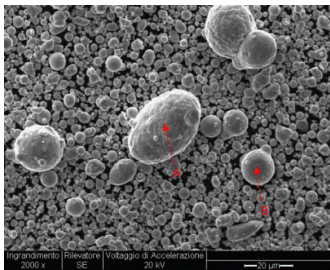
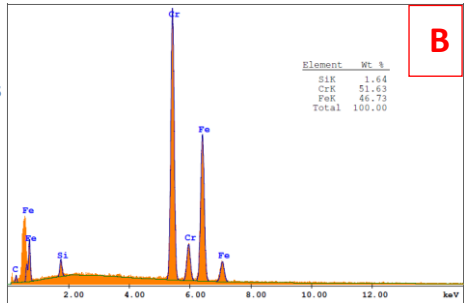


Figure 43. SEM images of the 430 master alloy powders.

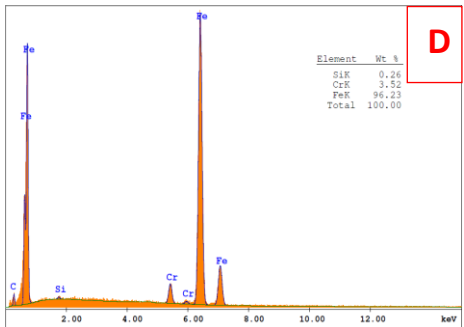
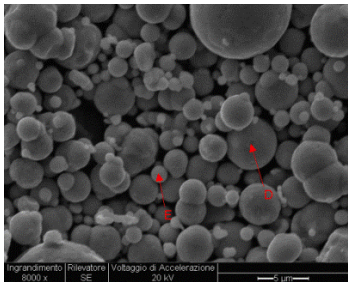


A

Figure 44. The spot analysis performed on two coarse particles.

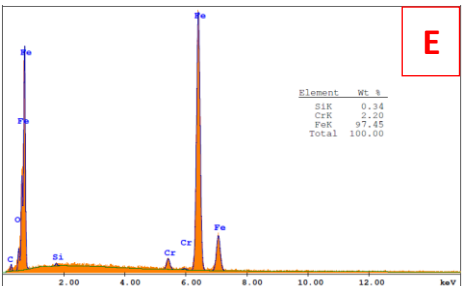


B



D

Figure 45. Spot analysis on carbonil iron particles.



E

The composition of the feedstock is confirmed by analyses: a carbonyl iron powder and a master alloy with the balanced content of chromium.

4.3.2 Dilatometry test

Figures 45 and 46 shows the dilatometric records of the two materials and the differential dimensional change curve, respectively. Again the isothermal sintering temperature is 1300°C.

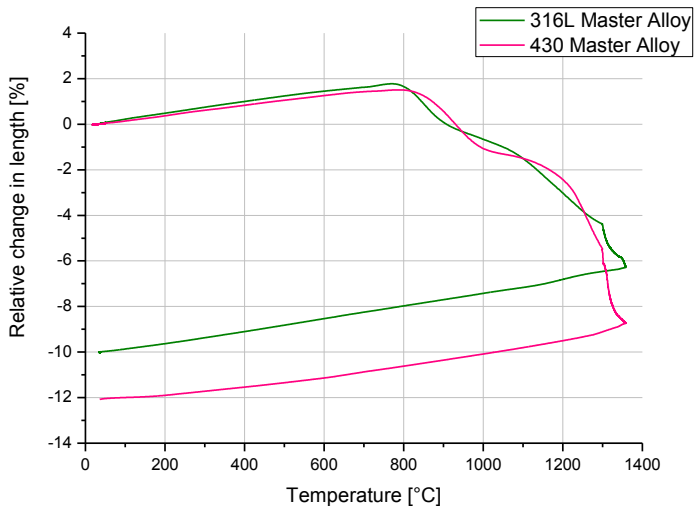


Figure 46. Relative change in length plot of the dilatometry test for the complete prealloy route.

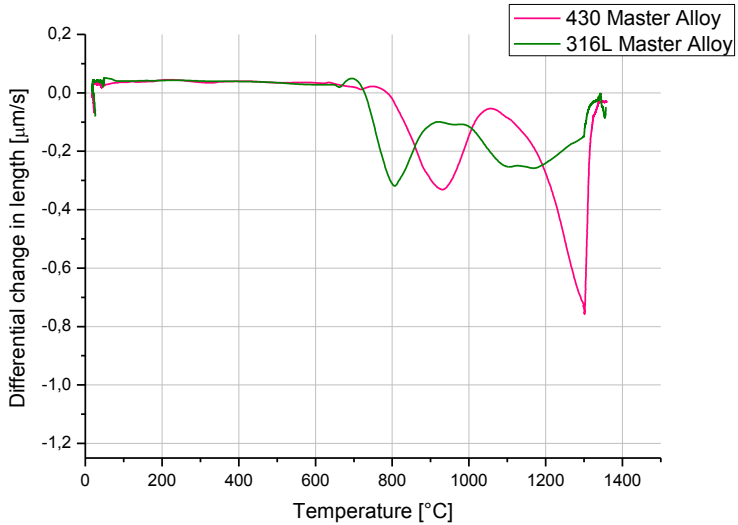


Figure 47. Differential change in length plot of the dilatometry test for the complete prealloy route.

The two figures show that the shrinkage during sintering is similar between these two feedstocks. In this way the mismatch is minimized. The stress arising during the whole of the sintering step (heating and isothermal holding) was calculated, and it is shown in figure 47.

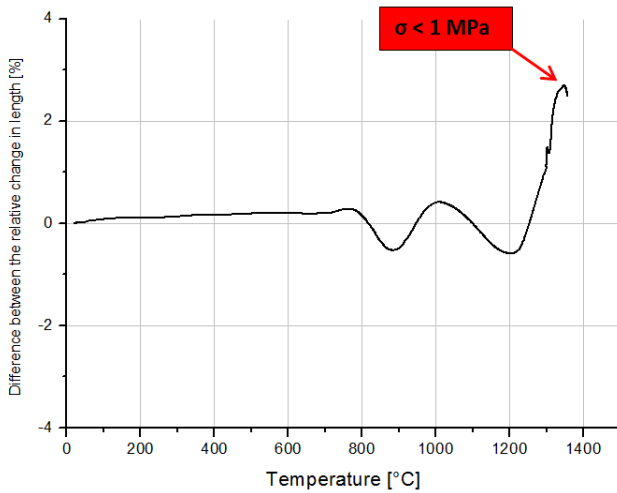


Figure 48. Calculated stress during the cosintering.

As the mismatch is lower respect to the other studied cases the stress is much lower. A stress lower than 1 MPa was calculated, that should be tolerated by the material without cracks.

No cracks were indeed observed, neither after sintering by visual inspection of the parts, nor after metallographic preparation. Figure 48 shows an example of the microstructure; the interface between the two parts is clearly visible, without any crack.

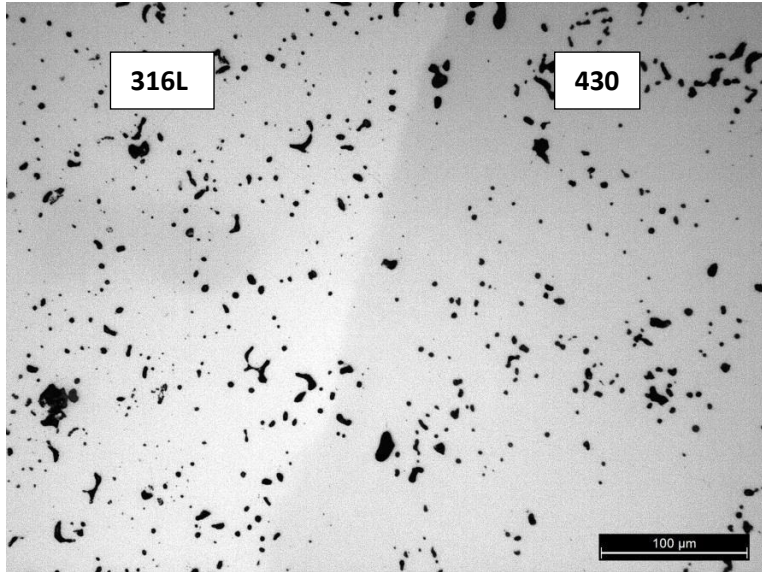


Figure 49. Metallographic image of the interface zone. No cracks are present and the two steels are perfectly joined.

4.4 Calculation of the ACSI

The ACSI values were calculated after dilatometry for all the three studied cases, in order to verify if even with such a complex geometry the ACSI route can give an idea of the feasibility of the co-injection and co-sintering. Results are reported in figure 49, where the dotted horizontal line shows the threshold above that co-sintering is expected to be unfeasible. An ACSI value of 15 is indeed considered as the upper limit to obtain a successful co-sintering.

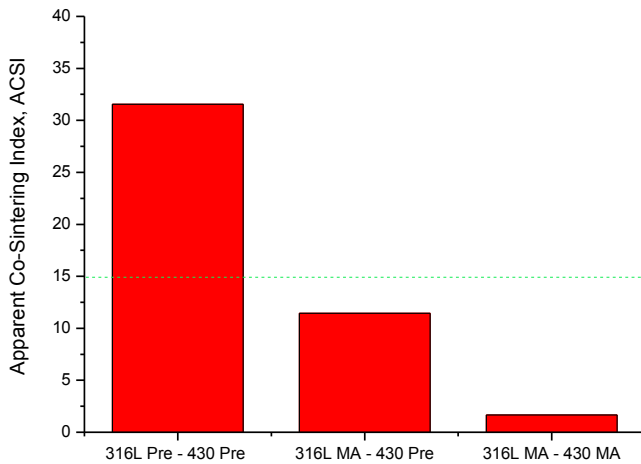


Figure 50. ACSI index for the three studied cases.

The values of the ACSI index in the studied cases decrease from 32, for the complete prealloy route, down to 10 in the prealloy/master alloy route and further down to around 2 for the complete master alloy route. Cracks are avoided only in this last studied case,. For the studied component the complexity of the geometry has a sensible effect on the acceptable mismatch between the co-sintered feedstocks and the threshold at 15 is not reliable. To obtain a component free from cracks or delamination is necessary to reduce such a limit down to 5-6.

4.5 Dimensional changes

With the purpose to further confirm the good matching of dimensional changes predicted by dilatometry tests, the two parts were sintered separately, and dimensional changes were measured with a CMM machine. The diameters indicated in the figures 50 and 51 for the 430 steel and 316L steel parts, respectively, were measured. . The dimensional changes measured here are related to the single parts, free to move during sintering without any reciprocal constrain. The machine makes a scan measuring many points on the same diameter; points are then used for the reconstruction of the circle with a best fit calculation. The 430 alloy part was measured in 7 positions at different heights (figure 50). The measurement shows that in the green state the walls of the cylindrical part are conic; this is made with the purpose of improving the extraction of the brown part from the mold. After sintering in almost all calculated diameter the standard deviation of the diameters is increased, but the shrinkage is very similar, as shown in Table 4.

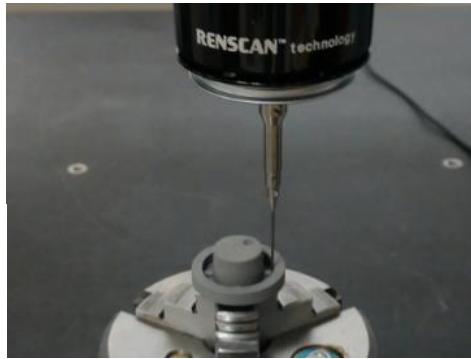
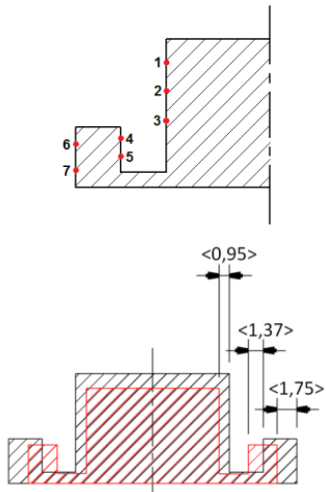


Figure 50. CMM machine measuring the 430 ring and drawings of the section with the measured points and average Δr (mm).

Measured diameter	Green [mm]	Sintered [mm]	$\Delta\phi$
ϕ_1	$13,673 \pm 0,075$	$11,735 \pm 0,081$	-14,17
ϕ_2	$13,846 \pm 0,167$	$11,953 \pm 0,047$	-13,67
ϕ_3	$14,017 \pm 0,017$	$12,142 \pm 0,121$	-13,38
ϕ_4	$19,970 \pm 0,030$	$17,181 \pm 0,319$	-13,97
ϕ_5	$19,933 \pm 0,067$	$17,222 \pm 0,278$	-13,60
ϕ_6	$25,931 \pm 0,069$	$22,388 \pm 0,194$	-13,66
ϕ_7	$25,982 \pm 0,018$	$22,513 \pm 0,215$	-13,35

Table 4. Measured diameters on both green and sintered 430 part.

For the 316L ring four diameter were measured.

Figure 51 shows the positions where diameters are measured in the 316L part, and table 5 summarizes the results.

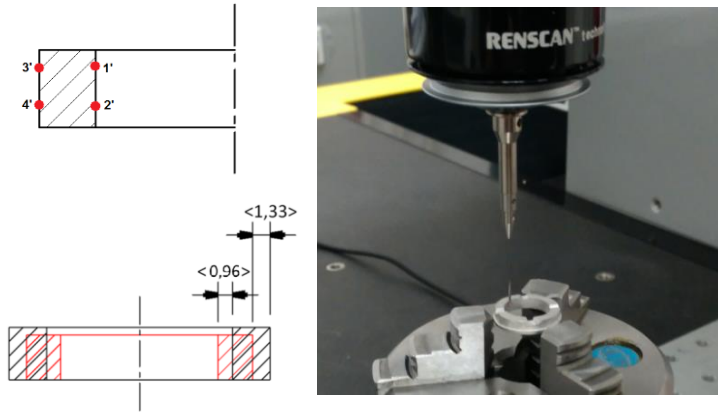


Figure 5151. CMM machine measuring the 316L ring and drawings of the section with the measured points and average Δr (mm).

Measured diameter	Green [mm]	Sintered [mm]	$\Delta\phi$
$\phi_{1'}$	$14,221 \pm 0,199$	$12,318 \pm 0,126$	-13,38
$\phi_{2'}$	$14,306 \pm 0,321$	$12,374 \pm 0,095$	-13,50
$\phi_{3'}$	$20,095 \pm 0,044$	$17,451 \pm 0,364$	-13,16
$\phi_{4'}$	$20,174 \pm 0,123$	$17,502 \pm 0,278$	-13,24

Table 5. Measured diameters on both green and sintered 316L part.

The comparison between dimensional changes is presented in figure 52, where the dimensional change of the radii (difference between the green and the sintered parts) is plotted versus the radius.

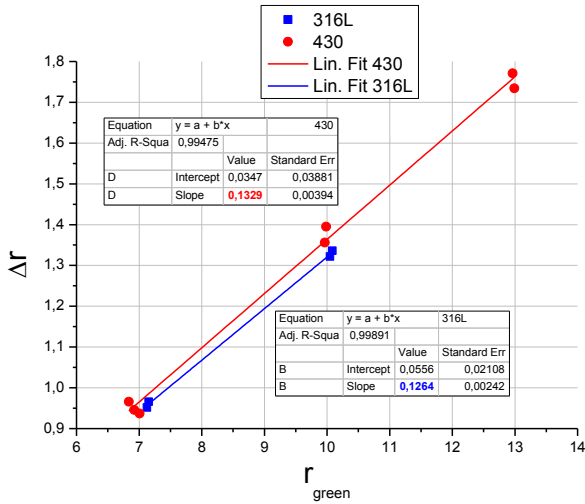


Figure 52. Δr (mm) vs. r (mm) plot of the points measured before and after sintering for the two steels rings.

The decrease of the internal radius is definitely the same for the two components, while that of the intermediate one is slightly greater for the ferritic steel than the austenitic one. These results confirm what observed by dilatometry tests. Along the inner interface, non differential dimensional change is observed, while the slightly higher contraction of the ferritic steel along the outer interface cannot cause the formation of defects. The diameters after sintering the two components molded together was measured with the CMM but only a few diameters of the co-injected component after sintering were measurable. The measurement on the entire co-injected part after sintering were made only on the external

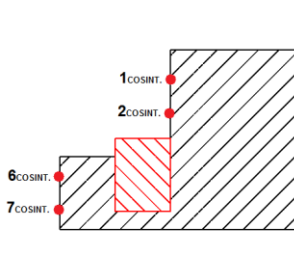
diameters that could be reached by the tip of the instrument, and results are reported in figure 53 and in table 6.

Measured diameter	Co-sintered part [mm]	Corresponding measure 430 free [mm]
$\varnothing_{1\text{COSINT}}$	$11,506 \pm 0,444$	$11,735 \pm 0,081$
$\varnothing_{2\text{COSINT}}$	$11,656 \pm 0,294$	$11,953 \pm 0,047$
$\varnothing_{6\text{COSINT}}$	$22,392 \pm 0,342$	$22,388 \pm 0,194$
$\varnothing_{7\text{COSINT}}$	$22,365 \pm 0,315$	$22,513 \pm 0,215$

Table 6. Measured diameters on the cosintered component and the 430 ring.



Figure 53. CMM machine measuring the complete co-sintered component.



Results show that the dimensional change of the outer diameters are the same in the co-sintered part and in the single one, as a further confirmation of the excellent matching of dimensional changes of the two materials.

4.6 Microstructure

The sample produced via complete master alloy route was analyzed to observe the microstructure, in particular at the interface between the two steels that is influenced by interdiffusion. The two steels differ for Ni and Mo content, both being present in the 316L steel only; even chromium content is higher in the austenitic steel, but the difference between the two materials are very small.

The microstructure of the part is shown in figure 54 and, after metallographic etching, in figure 55.

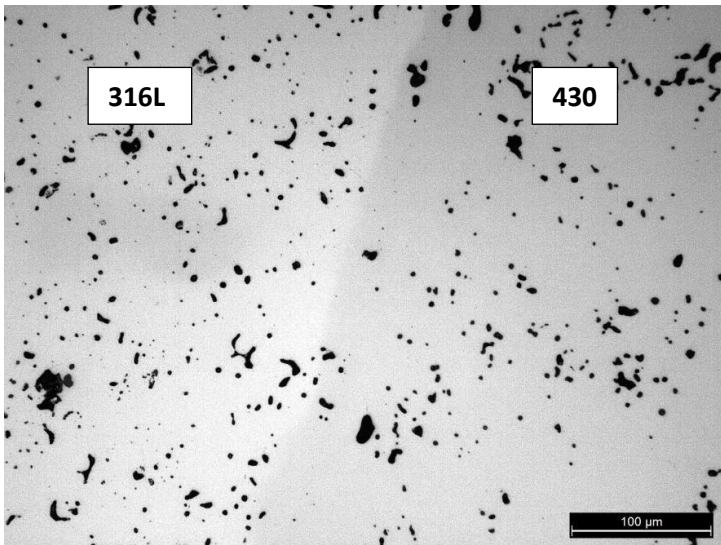


Figure 53. Interface zone after polishing.

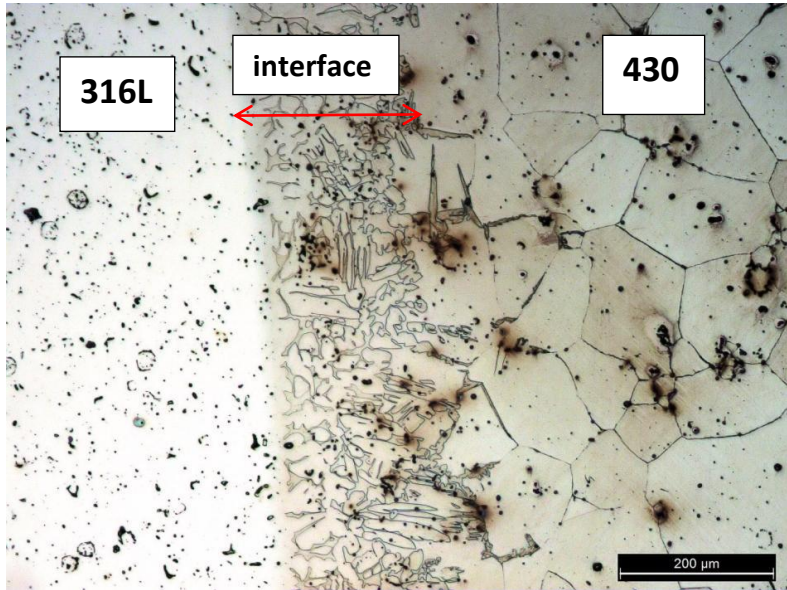


Figure 54. Microstructure of the interface revealed after etching using Vilella etchant.

A significant difference between the 316L and the 430 steels is visible just after polishing (fig. 54), related to the different residual porosity. The ferritic steel is more dense as it might be expected from the larger isothermal shrinkage measured during dilatometry tests. After etching the interface microstructure is revealed, as well as that of the 430 steel. The microstructure of the 316L can't be revealed because of the galvanic effect related to presence of the Ni-rich austenite of the 316 that is nobler than the 430. At the interface a new constituent is formed with a dual-phase

microstructure and a plate-like morphology on the 430 steel side [22].

Figure 56 shows the microhardness profile across the interface between the two steels.

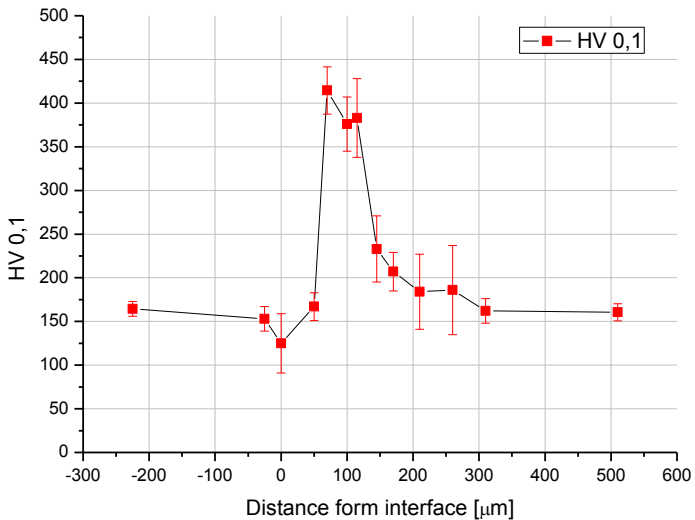


Figure 56. Microhardness measurement along the interface.

The microhardness profile across the interface constituent is quite scattered but it reveals a higher microhardness of the new constituent than both 316L and 430 steels. This may be attributed

both to the plate-like constituent that may be reasonably supposed being martensite.

4.7 Characterization of the interface constituent

In the specimens produced with the mixed feedstock the interface constituent appears as an almost continuous network with an irregular thickness, that makes its characterization rather complex. Some samples with a flat interface were co-injected and then sintered at two temperatures. In this way the diffusion occurs along one predominating direction, the morphology of the interface is more regular, as shown in figure 57 and the EDXS analysis is more truthful.

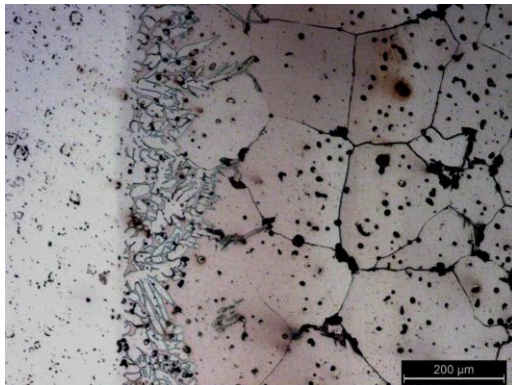


Figure 557. Non uniform thickness of the interface microstructure.

Figures 58 and 59 shows SEM images of the interface constituent after sintering without isothermal holding and with 1 hour holding at the sintering temperature, respectively.

1300°C – 0h

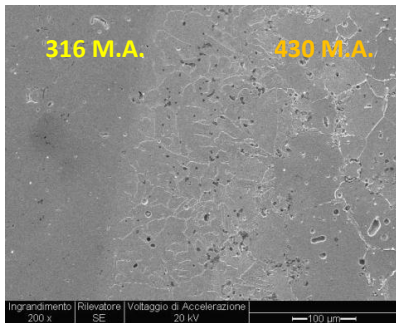


Figure 56. SEM image of the interface of the 0h case.

1300°C – 1h

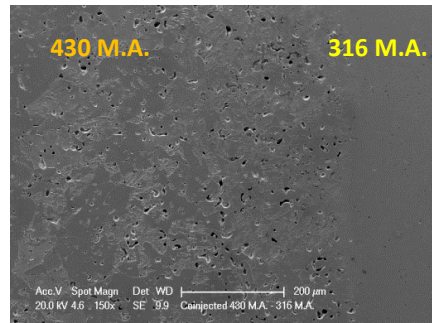


Figure 59. SEM image of the interface of the 1h case.

The difference is related to the thickness of the interface constituent. For the 0h case the thickness of the interface microstructure is around 150 μm, for the 1h case, as expected by a longer isothermal holding time, the thickness is around 300 μm. This means that a significant amount of the interface constituent is formed still during heating up to the sintering temperature.

A linescan analysis was made on the sample sintered for 1h isothermal holding and the result is shown in figure 60.

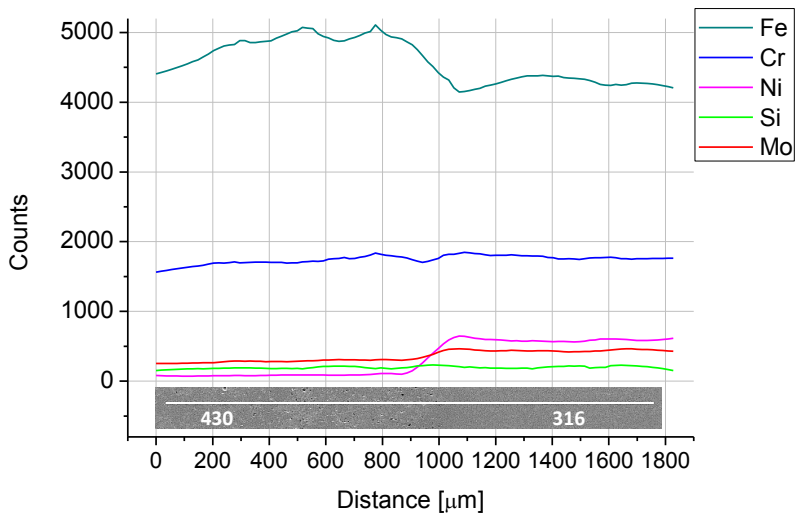
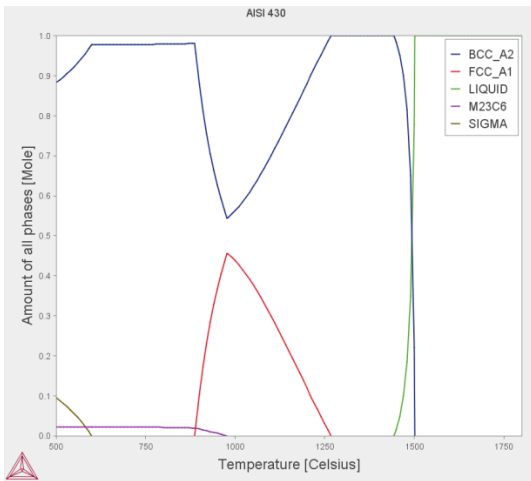


Figure 60. Linescan result across the interface of the 1h case.

The concentration profiles show that Nickel and Molybdenum diffuse from the 316L steel to the 430 one, as expected. An opposite diffusion of iron is also detected. The linescan plot shows also that the interdiffusion thickness is about 200 microns; in other cases, a larger thickness is detected, the mean value of the various measurements corresponding to the thickness observed on the metallographic images. .

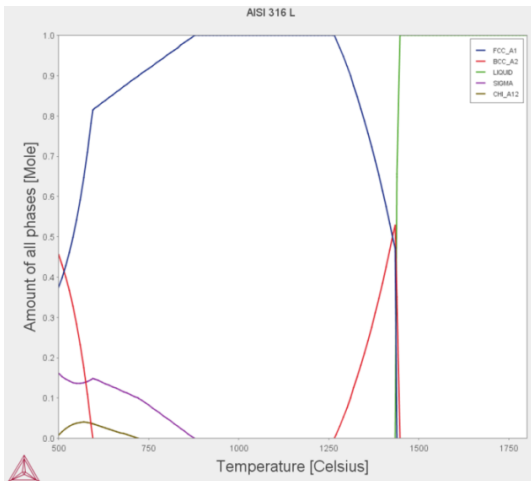
4.8 Thermo Calc and Dictra simulation

Figures 61 and 62 show the constitution of the two steels in the 500-1500°C temperature range, as predicted by ThermoCalc [23].



Temperature [Celsius]	Amount of FCC_A1 [Mole]	Amount of BCC_A2 [Mole]
1200	0.11992	0.88008
1210	0.10194	0.89806
1220	0.08406	0.91594
1230	0.06631	0.93369
1240	0.04869	0.95131
1250	0.03122	0.96878
1260	0.01390	0.98610
1268.09	0.00000E0	1.00000
1268.09		1.00000
1270		1.00000
1280		1.00000
1290		1.00000
1300		1.00000
1310		1.00000
1320		1.00000
1330		1.00000
1340		1.00000
1350		1.00000
1360		1.00000
1370		1.00000
1380		1.00000
1390		1.00000
1400		1.00000

Figure 61. Amount of phase vs. temperature by Thermocalc simulation for the 430 steel.



Temperature [Celsius]	Amount of FCC_A1 [Mole]	Amount of BCC_A2 [Mole]
1200	1.00000	
1210	1.00000	
1220	1.00000	
1230	1.00000	
1240	1.00000	
1250	1.00000	
1260	1.00000	
1265.0	1.00000	
1265.0	1.00000	8.65627E-15
1270	0.99007	0.00993
1280	0.96936	0.03064
1290	0.94745	0.05255
1300	0.92428	0.07572
1310	0.89982	0.10018
1320	0.87403	0.12597
1330	0.84687	0.15313
1340	0.81829	0.18171
1350	0.78826	0.21174
1360	0.75672	0.24328
1370	0.72363	0.27637
1380	0.68895	0.31105
1390	0.65263	0.34737
1400	0.61462	0.38538

Figure 62. Amount of phase vs. temperature by Thermocalc simulation for the 316L steel.

At the sintering temperature all the volume of the 430 is composed by ferrite, while that of the 316L is composed mainly by austenite (92,5%) with a small amount of delta ferrite (7,5%). To simplify the Dictra simulation, this steel was considered as fully austenitic. Only the main elements (Fe, Cr, Ni, Mo) were used for the simulation and the analysis

In figures 63 and 64 the concentration profiles of the elements across the interface are plotted for 0 and 1 hour isothermal holding at 1300°C, respectively.

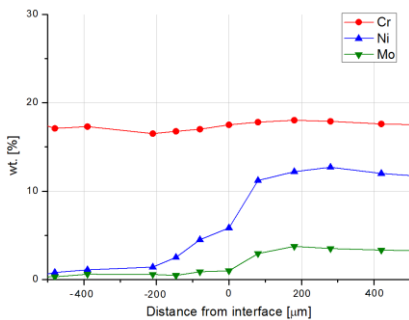


Figure 63. Concentration profile of elements across the interface for the 0h case.

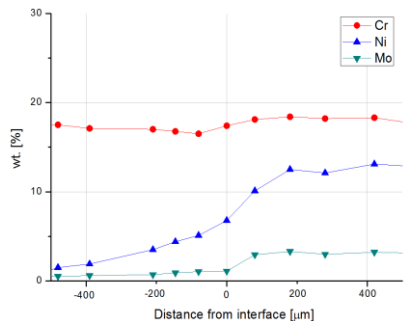


Figure 64. Concentration profile of elements across the interface for the 1h case.

The concentration profiles collected by EDXS spot analysis were then compared with the Dictra simulations in figures 65 and 66 for the 0h and 1h cases, respectively. The original position of the interface corresponds in both cases to the value 30 on the X axis.

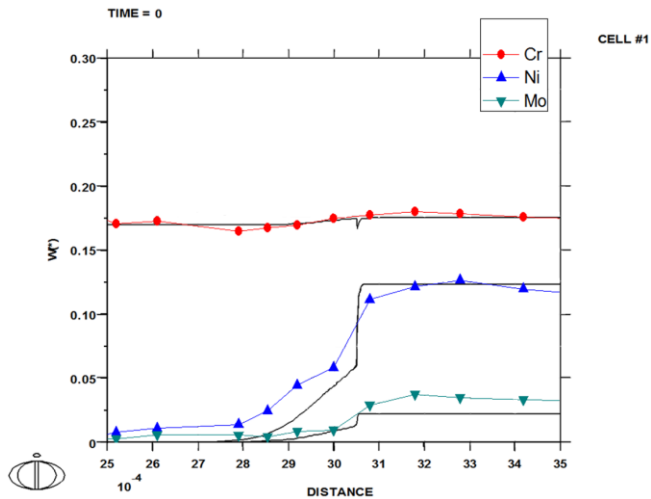


Figure 65. Dictra simulation plot compared with the spot analysis collected across the interface for the 0h case.

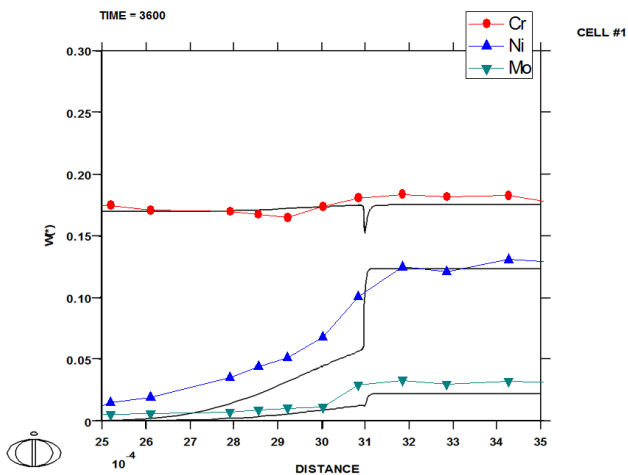


Figure 57. Dictra simulation plot compared with the spot analysis collected across the interface for the 1h case.

In both cases, the measured diffusion depth of Ni and Mo is greater than that predicted by Dictra (around 150 μm greater after 1 hour at 1300°C); moreover, Dictra predicts a sharp gradient. This discrepancy may be attributed to:

1. the effect of porosity that promotes surface diffusion in addition to the bulk one;
2. the deviation from the perfectly flat interface shape, due to the interpenetration of the powder particles of the two steels during co-injection

Both these effects cannot be easily implemented in Dictra modeling. Dictra shows that the layer interested by diffusion is thicker in ferrite than in austenite, and this is due to the greater diffusivity of the alloying elements in the bcc lattice of ferrite than in the fcc of austenite. The comparison between theoretical predictions and experimental data show that Dictra software can be a good help in understanding the diffusion phenomena, but it fails in predicting the real diffusion depth due to the particular morphology of the interface.

The Ni diffusion from the austenitic steel to the ferritic one causes a depletion in the former, that may destabilize austenite. The formation of both ferrite and martensite from the unstable austenite may occur, during isothermal holding and on cooling, respectively. On the other side, the Ni enrichment of ferrite in 430

steel may cause the formation of some austenite during isothermal holding, that may transform in martensite on cooling.

To interpret the microstructure of the interface constituent, the results of the quantitative analysis reported in figure 66 are reported in the Schaeffler diagram, as shown in figure 67 [18].

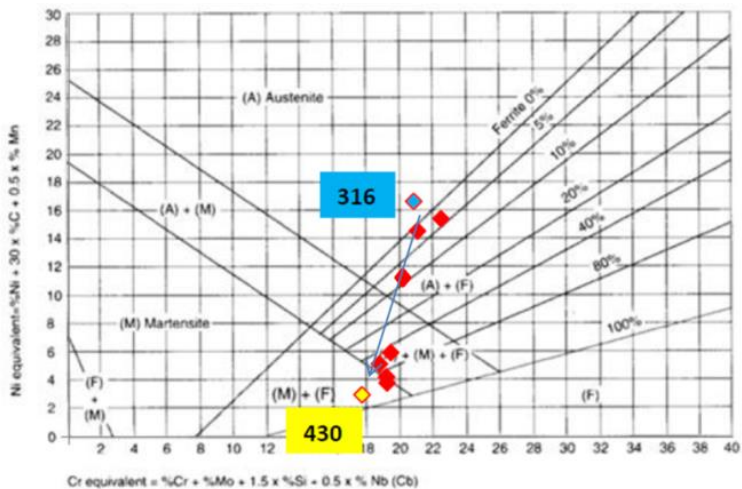


Figure 67. Spot analysis compared to the Schaeffler diagram for phase content at room temperature.

The Schaeffler diagram indicates that on moving from austenite to ferrite the microstructure of the interface constituent evolves from a dual-phase ferrite/austenite to a dual-phase ferrite/martensite. These indications are coherent with the morphology of the interface

constituent, that shows a typical dual-phase microstructure close to austenite and a plate-like microstructure close to ferrite, figure 68.

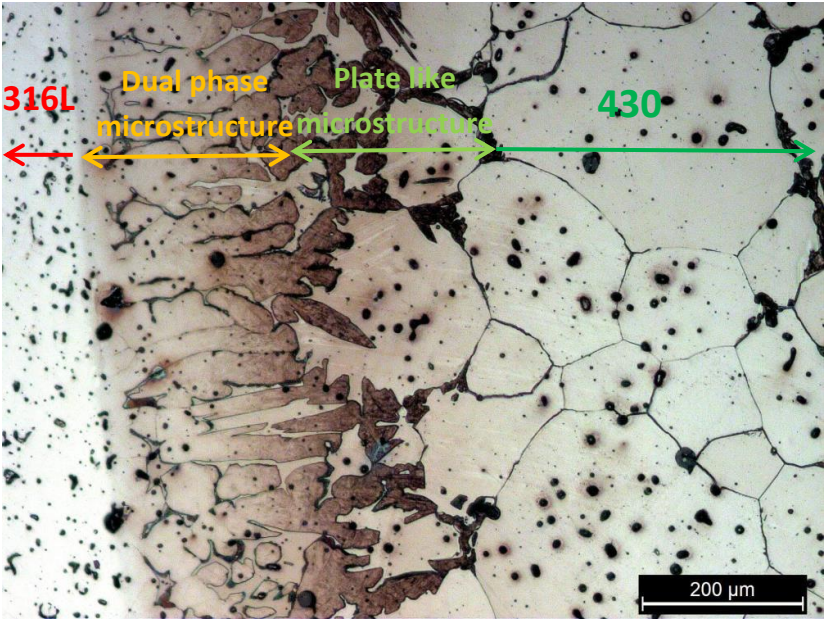


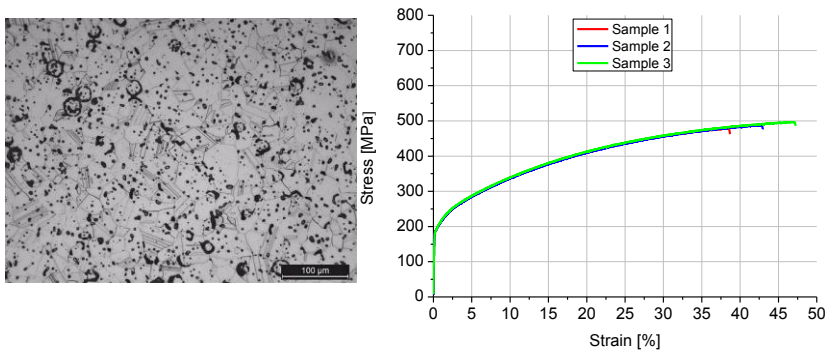
Figure 68. Morphology of the interface passing from the austenitic to the ferritic steel.

4.9 Mechanical properties

Tensile tests were performed on the samples sintered at 1300°C with 1h isothermal holding.

316L

Figure 69 shows the microstructure, the tensile stress-strain curves of three specimens and the resulting tensile properties, along with density of the austenitic stainless steel.



Aisi 316L – 1h	
Density [%]	93,7 ± 0,2
σ_y [MPa]	188 ± 1
σ_{max} [MPa]	491 ± 10
ϵ_{max} [%]	43,0 ± 4,2

Figure 69. Microstructure, stress-strain curve and density of the 316L.

The results show the expected yield strength, as well as quite a large percent elongation and also a noticeable strain hardening. The plastic deformation is only uniform, likely because of the presence of pores that do not allow the localized deformation [24]. Nevertheless UTS is as expected.

430

Figure 70 shows the microstructure, the tensile stress-strain curves of three specimens and the resulting tensile properties, along with density of the ferritic stainless steel.

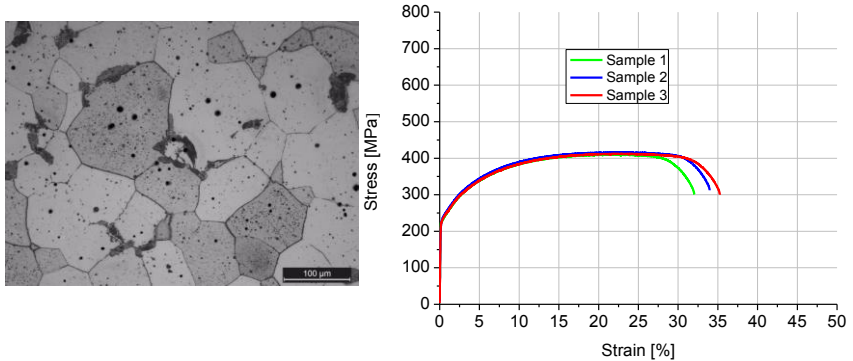


Figure 70. Microstructure, stress-strain curve and density of the 430.

In the case of the 430 steel some localized plastic deformation is observed, that may be due to the very low porosity that does not affect the tensile behavior significantly. The whole of the tensile properties are as expected.

MIX – 1h

Figure 71 shows the microstructure, the tensile stress-strain curves of three specimens and the resulting tensile properties, along with

density of the steel produced with the mixed feedstock, to evaluate the mechanical properties of the interface constituent in the real component.

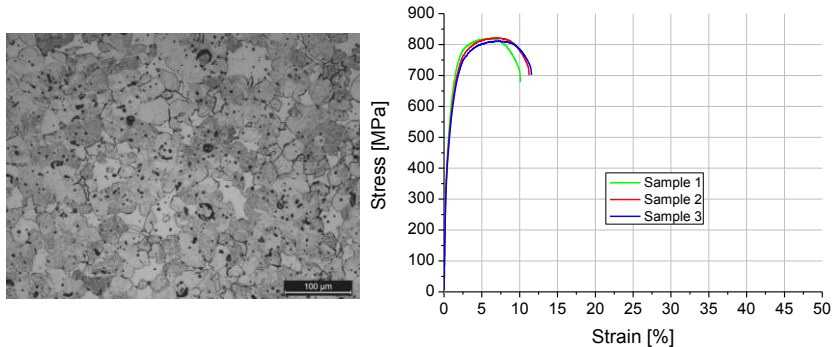


Figure 71. Microstructure, stress-strain curve and density of the MIX.

The yield stress is much higher respect to the original two feedstocks, the stress increases immediately during the initial part of the plastic deformation reaching a very high tensile strength. Localized plastic deformation is observed, too, and the tensile strain at fracture indicates quite a good ductility. The tensile behavior is very different from that of the two starting materials, not representing a combination of the two ones. Such a behavior may be attributed to the finer and dual-phase microstructure and to the presence of martensite. Due to the Ni depletion of austenite, a TRIP effect might occur. X-ray Diffraction was then carried out on the

specimen before and after the tensile test to quantify the phases. Results are reported in table 7.

	% vol before tensile test	% vol after tensile test
α -Fe	81 \pm 1	82 \pm 1
γ -Fe	19 \pm 1	18 \pm 1

Table 7. results of XRD analyses on the 50/50 feedstock after 1h sintering at 1300°C

The amount of austenite is much smaller than the starting one (in the mixed feedstock) just after sintering, due to the destabilization of austenite. Ferrite and martensite cannot be resolved by XRD, as well known.

No phase transformation occurs during the tensile test, that means TRIP effect is not responsible for the great strain hardening.

The plastic field of the stress-strain curves of the three steels was elaborated in terms of true stress – true strain diagrams, and the agreement with some strain hardening models was verified. Results are shown in figures 72 to 74

316 – 1h

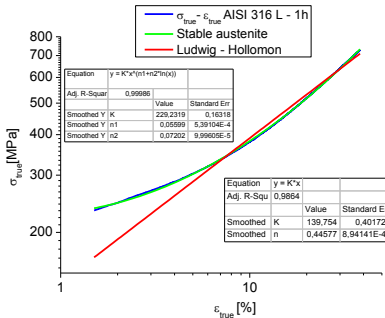


Figure 72: log-log true stress- true strain diagram of the 316L steel.

The $\sigma_{TRUE}-\epsilon_{TRUE}$ plot is perfectly fitted by the model, valid for the strain hardening of the stable austenite.

430 – 1h

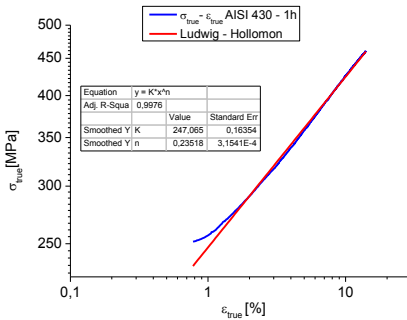


Figure 73. Log-log true stress-true strain diagram of the 430 steel

The $\sigma_{TRUE}-\epsilon_{TRUE}$ plot in this case is fitted by the Ludwig-Hollomon equation revealing the typical strain hardening behavior of the ferrite.

MIX – 1h

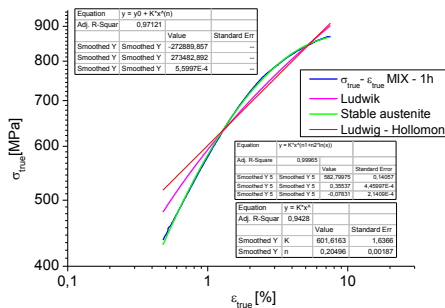


Figure 74. Log-log true stress-true strain diagram of the MIX steel

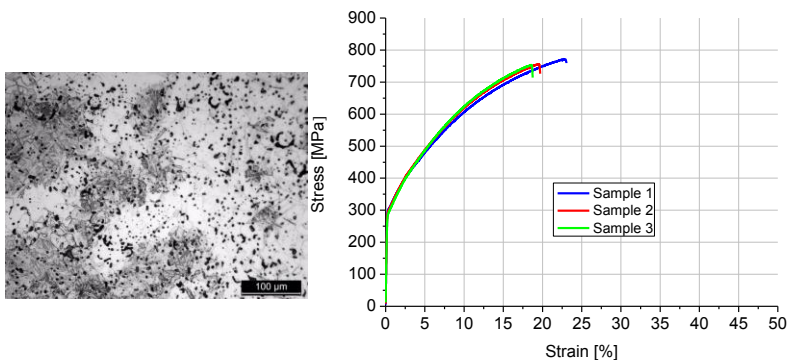
The $\sigma_{TRUE}-\epsilon_{TRUE}$ plot in this case is fitted by model, valid for the strain hardening of the stable austenite.

The strain hardening model of the mixed steel is represented by equation proposed for a stable austenite. This means that even a low amount of austenite (around 20%) is able to determine the plastic deformation of the material.

The mechanical test results of the 316L and the 430 sintered with the isothermal holding time of 1 hour are aligned with the expected values and behaviors for these steels. The high strength, good ductility and in particular way the evolution of mechanism related to the plastic deformation exhibited during the tensile test of the steel produced with the MIX feedstock, i.e. of the interface constituent in the final component, can be related to the fine dual-phase microstructure and to the presence of martensite.

Since the destabilization of austenite occurs during the sintering cycle, tensile specimens with different holding time at the sintering temperature were produced, to investigate the deformation behavior.

Figure 75 shows the microstructure, the tensile stress-strain curves of three specimens and the resulting tensile properties, along with density of the steel produced with the mixed feedstock without isothermal holding at 1300°C.



Mix 1300°C – 0h	
Density [%]	94,4 ± 0,1
σ_y [MPa]	300 ± 6
σ_{max} [MPa]	763 ± 14
ϵ_{max} [%]	20,5 ± 2,3

Figure 75. Microstructure, stress-strain curve and density of the mix steel sintered 0h.

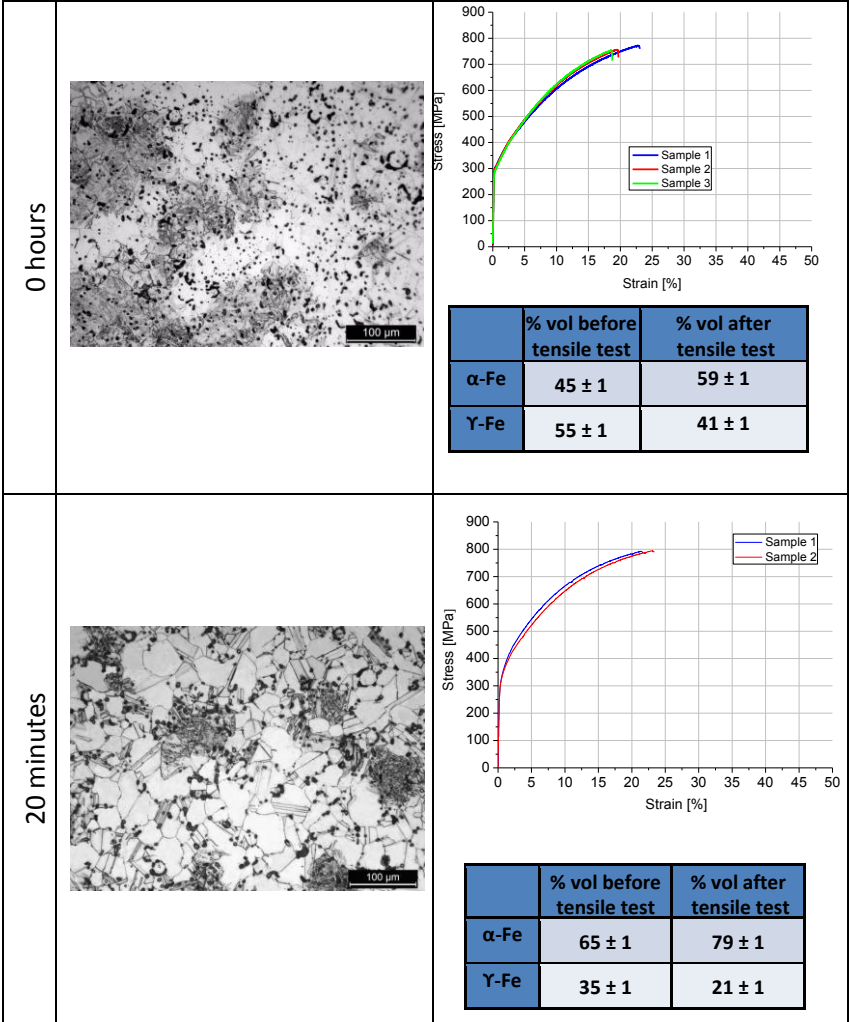
The microstructure shows a smaller amount of the microstructural constituent produced by interdiffusion. The tensile stress-strain curves displays a significant strengthening with respect to the two base steels, even if strength is lower than that of the materials sintered 1 hour. Ductility is correspondingly higher.

Table YY reports the results of XRD analysis. The starting content of austenite is 55%, i.e. the same as the starting feedstock, indicating that no martensite is formed after heating up to the sintering temperature. However, it decreases after the test down to 41%. A TRIP effect involving about 30% of austenite occurs during plastic deformation, indicating that austenite has been partially destabilized against the strain induced transformation, due to Ni depletion.

	% vol before tensile test	% vol after tensile test
α -Fe	45 ± 1	59 ± 1
γ -Fe	55 ± 1	41 ± 1

Table 7. results of XRD analyses on the 50/50 feedstock after 1h sintering at 1300°C

Figure 76 shows the sequence of the microstructures and of the tensile stress-strain curves on increasing isothermal holding time from 0h to 1h.



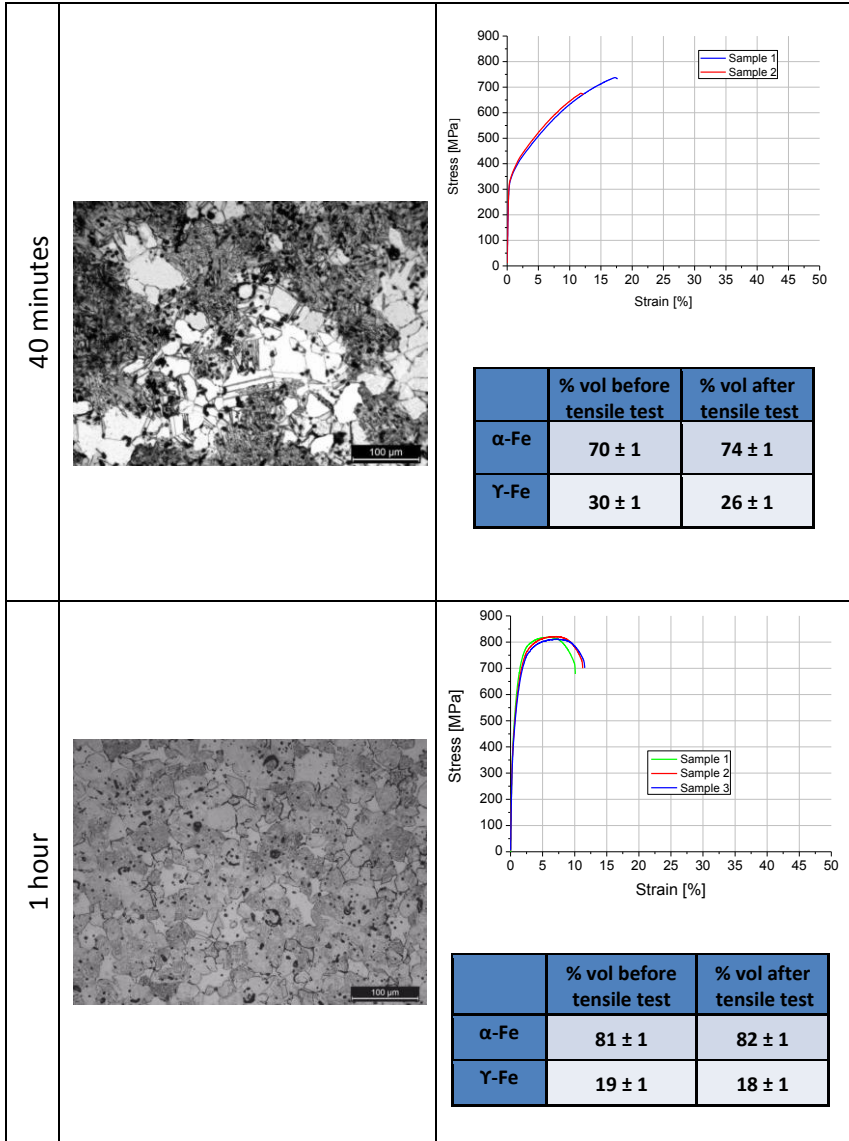


Figure 76. Microstructures and of the tensile stress-strain curves on increasing isothermal holding time from 0h to 1h.

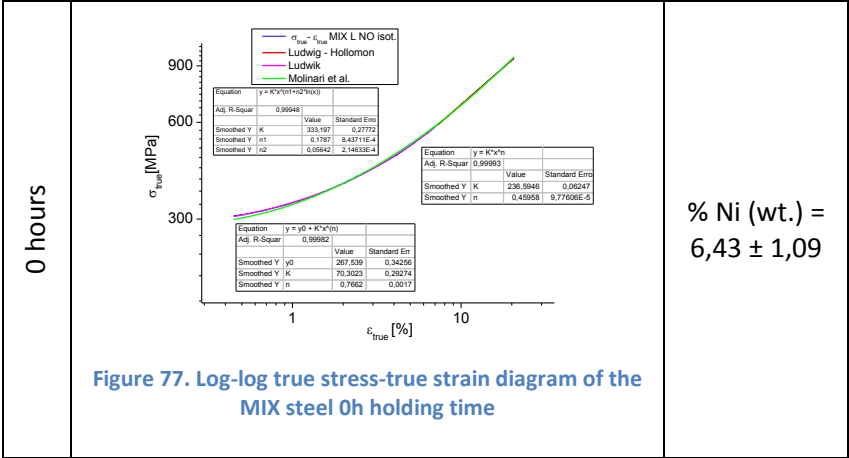
On increasing holding time up to 20 and 40 minutes, the amount of austenite decreases, indicating that the further Ni depletion lead to enhanced destabilization, resulting in the formation of martensite on cooling [25 – 27]. The remaining austenite transform into martensite during plastic deformation (TRIP) but the in a less quantity on increasing time from 20 to 40 minutes. This means that the remaining austenite tends to result increasingly stable against the strain induced transformation. After 60 minutes, the remaining austenite is quite low, but definitely stable against the TRIP effect.

These results cannot be easily interpreted. It seems that on increasing the holding time the material evolves from one stable condition (stable austenite) towards another stable conditions characterized by a less content of stable austenite. This evolution occurs through a transient during which a portion of austenite, involved in the interdiffusion process, is progressively destabilized by a continuous Ni depletion.

Stability of austenite depends on two temperatures: M_d (stability respect to the strain induced transformation) and M_s (stability respect to martensite transformation on cooling). Both temperatures depend on the Ni and Mo content, being lower than room temperature in the starting material. M_d is higher than M_s . On decreasing Ni and Mo content, first M_d increases above room temperature, activating strain induced transformation; afterwards, even M_s results higher than room temperature, activating martensite transformation on cooling. Such a sequence occurs in the interdiffusion layer on increasing holding time.

It's rather interesting the observation that the plastic field of the 0h holding time material is well fitted by both the model for stable

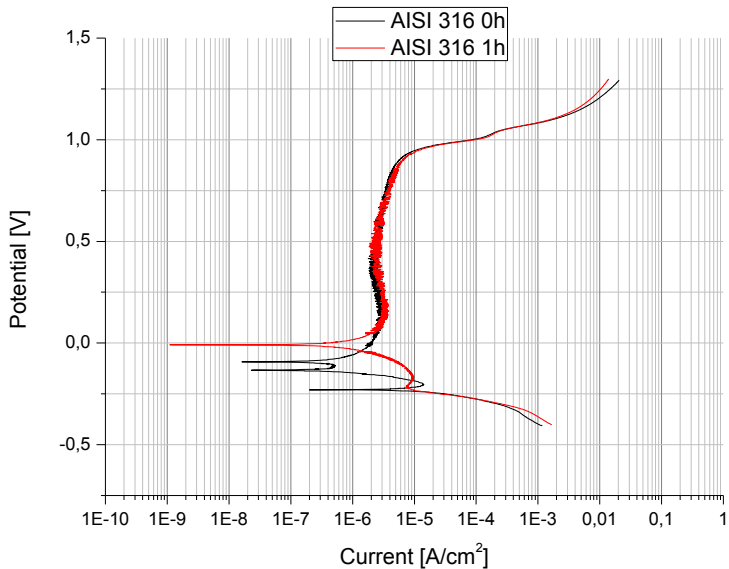
austenite and the Ludwick equation, well suitable to represent the TRIP mechanism, as shown in figure 77.



4.10 Corrosion resistance

316L

Figure 78 represents the potentiodynamic curves of the samples of 316L sintered for 0h and 1h of isothermal holding time and the values of the significant parameters.



	E_{corr} [mV]	E_p [V]	I_p [$\mu\text{A}/\text{cm}^2$]	E_t [V]
316L – 0h	-93,0	0,02	2,40	0,93
316L – 1h	-8,9	0,07	2,40	0,93

Figure 79. Potential curves for the 316L sample sintered 0h and 1h isothermal holding time and calculated values.

The curves of the 316L in the two conditions are very similar. The difference in porosity is not relevant for the passivation of the metal.

For both the curves the passivity nose is not present because of a preexisting passivation layer on the surface of the sample. A slight difference between the two samples is observed for the E_{corr} , that is a little bit higher for the 316L-1h.

In figure 79 SEM images of the surfaces after the test are shown, presenting the typical morphology of a uniform corrosion.

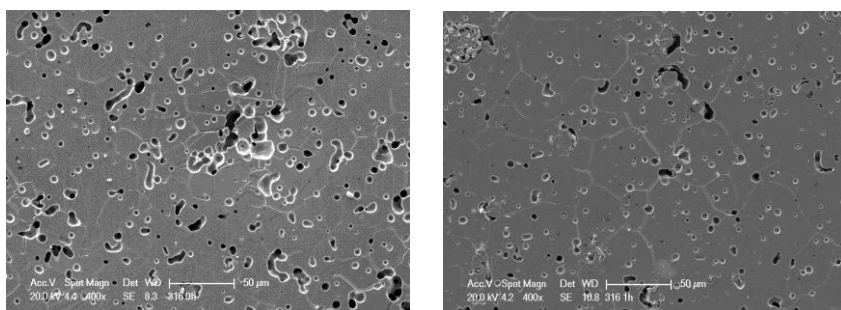
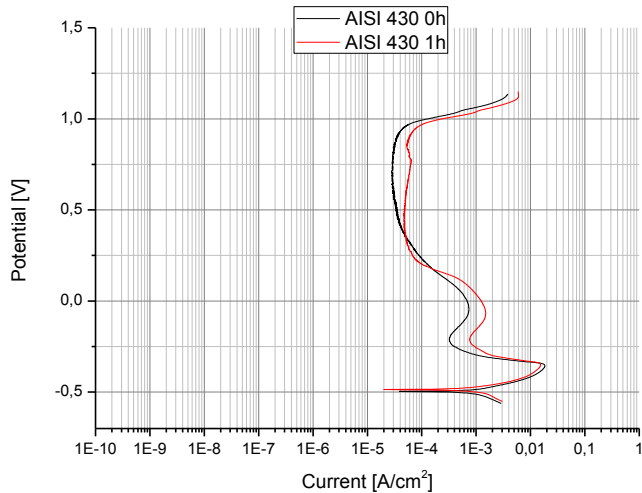


Figure 79. 316 L samples surfaces after the test: 0h (left) and 1h (right) isothermal holding

430

Figure 80 represents the potentiodynamic curves of the samples of 430 sintered for 0h and 1h of isothermal holding time and the value of the significant parameters.



	E_{corr} [mV]	E_p [V]	I_p [$\mu\text{A}/\text{cm}^2$]	E_t [V]
430 – 0h	-496,4	0,32	28,8	0,92
430 – 1h	-486,3	0,24	47,2	0,86

Figure 80. Potential curves for the 430 sample sintered 0h and 1h isothermal holding time and calculated values.

The curves of the two 430 samples compared to the curves of the 316L show immediately a lower resistance to corrosion of this steel in the specific used solution, represented by a lower value of the E_{corr} and a higher valued of the I_p . In any case also the 430 has a passivity interval after the typical nose related to the formation of a protective oxide layer.

Figure 81 shows the corrosion morphology of the two materials, still representing the morphology of a uniform corrosion.

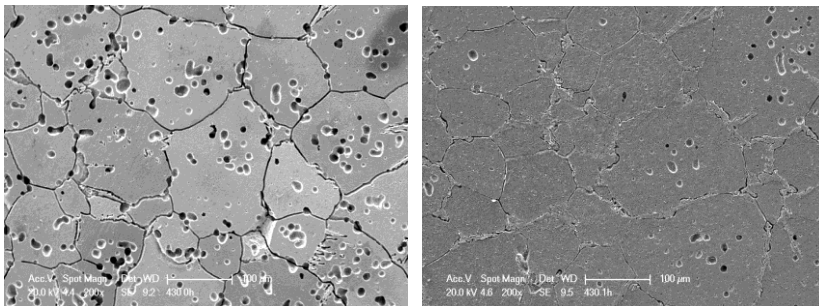
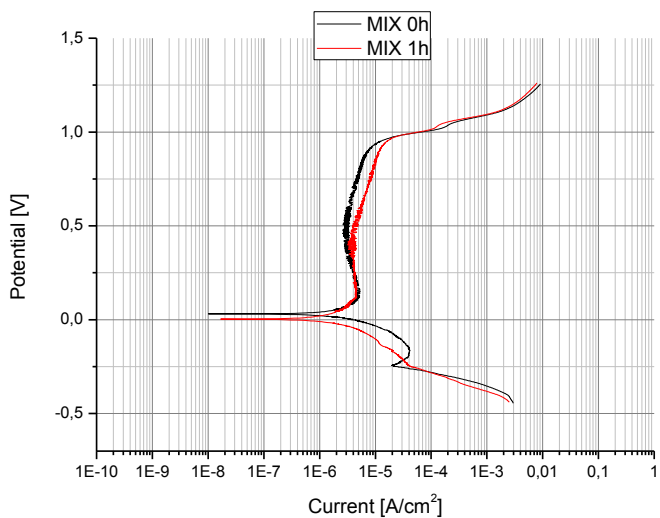


Figure 81. 430 samples surfaces after the test: 0h (left) and 1h (right) isothermal holding

MIX

Figure 82 represents the potentiodynamic curves of the samples obtained with the mixed feedstock sintered for 0h and 1h of isothermal holding time and the values of the significant parameters.



	E_{corr} [mV]	E_p [V]	I_p [$\mu\text{A}/\text{cm}^2$]	E_t [V]
MIX – 0h	30,9	0,11	3,92	
MIX – 1h	3,2	0,12	3,04	

Figure 82. Potential curves for the 430 sample sintered 0h and 1h isothermal holding time and calculated values.

The curves of the mix samples are very similar to the curves relative to the 316L. This is a very interesting result considering also the heterogeneous microstructure composed of ferrite, martensite and austenite . The explanations for this behavior may be as follows:

1. The martensite is formed by the depletion of the Ni rich austenite of the 316L that during cooling. The resistance to corrosion is in this way extremely good also for this constituent that is also under a compressive stress due to the expansion during the transformation.
2. Both the 316L and 430 are steels that have a passivity interval, a galvanic effect coming from their coupling is limited also because the difference in E_{corr} is small. In any case the austenite and the martensite constituents can force an anodic reaction on the ferrite surface that develops the protective oxide layer, so it reaches faster a passivity.

The presence of the ferrite, considered a weaker constituent to corrosion, is balanced by the other two constituent and the limited galvanic effect helps the ferrite and the good result of the MIX steel in the potential tests.

Figure 83 shows the corrosion morphology of the two materials.

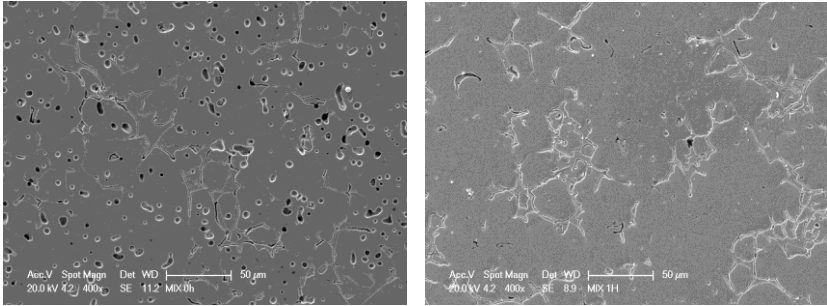


Figure 83. 430 samples surfaces after the test: 0h (left) and 1h (right) isothermal holding.

No evidence of localized corrosion attack is observed, a part the localization at the interface between austenite and ferrite/martensite[28]. However, this localized attack is shown after the breakdown of the protective oxide layer promoted by the increase in the voltage. In figure 84 all the curves are shown to highlight the excellent corrosion resistance of the mixed constituent that will be produced at the interface between the two part in the real component.

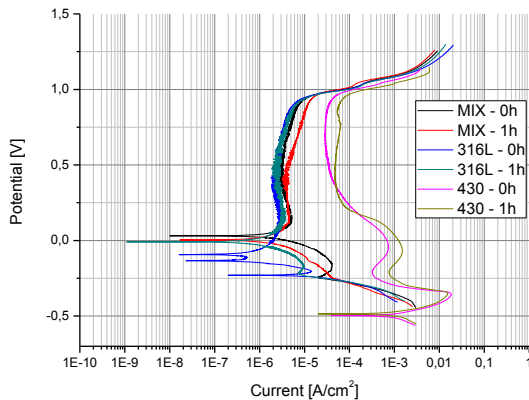


Figure 84. Potential curves for all the tested samples

5.0 Conclusions

In this work the production of an automotive fuel injection system by 2C-MIM of two stainless steels was investigated, in the frame of an industrial project in cooperation with Mimest SpA.

The first part of the work was focused on the study of co-sintering of two co-injected feedstocks. Dilatometry tests on different powders were performed to individuate the best solution to minimize the differences in the shrinkage behavior during the thermal cycle, the achieved results may be summarized as follows:

- The complete prealloy route is affected by the slower self-diffusion of iron into the f.c.c lattice of the 316L respect to the b.c.c lattice of the 430. The shrinkages starts at different temperatures generating a stress at the interface that is not acceptable. The final part presents cracks and delamination.
- A hybrid prealloy/ master alloy route is anyhow not feasible. The difference in powder size makes these powders not compatible. Shrinkage behavior is still quite different, and indeed cracks are still visible at the interface between the two steels.

- The complete master alloy route is the solution to obtain a uniform shrinkage between the two powders during sintering. The final part is not affected by any crack.

An ACSI index was calculated for each of the matches. Due to the complexity of the geometry studied in this work, to produce a not defected component, it's necessary to obtain an ACSI index lower than 5.

During co-sintering, a new microstructural constituent is produced at the interface between the two materials due to interdiffusion. It has a complex microstructure that was investigated in depth in the second part of the work. The results may be summarized as follows:

- The interface microstructure is composed of different constituents: austenite, ferrite and martensite as the result of the diffusion of the alloying elements, Ni and Mo from the austenitic steel to the ferritic one, Fe on the opposite direction.
- EDXS analysis revealed that Nickel is the alloying element mainly subject to the diffusion as the gradient between the two steels is high. The diffusion depth is in the range of some hundreds of microns.

- DICTRA simulations can be a valid tool to estimate interdiffusion, but it is not reliable for the diffusion depth calculation due to the particular morphology of the interface between two materials in form of interpenetrating powders.
- Martensite is formed during cooling from the sintering temperature due to the transformation of the austenite that is less stable because of the nickel depletion after its diffusion toward the ferritic steel.
- From the EDXS analysis across the interface it is possible to determine the constituents that will be present at room temperature by the quantity of alloying elements compared with the Schaeffler diagram.
- The microstructural constituent obtained at the interface with 1h of isothermal holding time is mainly composed by martensite/ferrite; its tensile strength is much higher than that of the two base steels, and the tensile ductility is more than sufficient for any mechanical application.
- Also with no holding time (0h) the mechanical properties are satisfying. In this case a TRIP effect takes place allowing to obtain very high UTS and also a very good ductility.

- The longer is the isothermal holding time the lower is the quantity of austenite in the final microstructure of the interface and the higher the presence of martensite.
- Regarding corrosion resistance in the 0.5M H₂SO₄ solution the results were brilliant. The galvanic effect due to the coupling of the 430 and 316L helps the ferritic steel to develop the protective oxide layer enhancing its corrosion resistance. In this way the interface region has a corrosion resistance comparable to the one of the 316L. The limited differences of porosity between the samples sintered 1h respect to the ones sintered 0h are not sensible.

The production of this automotive component by the use of the 2C-MIM was demonstrated to be successful. After sintering the component obtained had no defects, good mechanical and corrosion resistance. The choice of the perfect matching powders, size distribution, chemical composition and microstructure is fundamental. All these parameters influences heavily the behavior during sintering and the stresses generated between the to part made of different steels. The diffusion of Ni is the main phenomena that affects the microstructure of the interface that was demonstrated to be composed of ferrite, martensite and austenite in varying content based on the isothermal holding time.

mechanical and corrosion resistance properties. The choice of the perfect matching powders, size distribution, chemical composition and microstructure is fundamental. All these parameters influences heavily the behavior during sintering and the stresses generated between the metals. The diffusion of Ni is the main phenomena that affects the microstructure of the interface that was demonstrated to be composed of ferrite, martensite and austenite in varying content based on the isothermal holding time.

6.0 Bibliography

- [1] Donald F. Heaney ; Woodhead Publishing; Handbook of metal injection molding; 2012
- [2] I. Todd, A.T. Sidambe; Chapter 6 - *Developments in metal injection moulding (MIM) Advances in Powder Metallurgy Properties, Processing and Applications*; pages 109-146
- [3] www.jangsutech.com
- [4] A.Bose, I. Otsuka, T. Yoshida, H. Toyoshima; *Faster sintering and lower costs with ultra-fine MIM powders*; Metal Powder Report, Volume 63, Issue 5, 2008, Pages 25-30

[5] R. German, A. Bose; *Injection Moulding of Metals and Ceramics*; MPIF, Princeton, USA, 1997.

[6] A. J Coleman, K. Murray, M. Kearns, T. A. Tingskog, B. Sanford; E. Gonzalez; *Effect of Particle Size Distribution on Processing and Properties of Metal Injection Moulded 4140 and 4340*.

[7] P. A. Davies, G. R. Dunstan, D. F. Henaey, T. J. Mueller; *Comparison of master alloy and pre-alloyed 316L stainless steel powders for metal injection molding (MIM)*; In Proc. Int. Conf. Powder Met. & Particulate Material, 2004.

[8] M-A, Porter, Master Thesis; *Effect on binder system for metal injection moulding*; Lulea University of Technology, Division of Engineering Materials.

[9] P. Setasuwon, A. Bunchavimonchet, A. Danchaivijit; *The effects of binder components in wax/oil systems for metal injection molding*; Journal of Materials Processing Technology 2008; vol. 196(1), pages 94-100.

[10] M.S. Huang, H.C. Hsu; *Effect of backbone polymer on properties of 316L stainless steel MIM compact* ; Journal of Materials Processing Technology; 2009, Volume 209, Issues 15-16, pages 5527-5535

[11] Catamold® Feedstock for Metal Injection Molding: Processing - Properties - Applications Technical Information BASF AG

[12] / Dominick v. Rosato, Donald v. Rosato, M. G. Rosato; *Injection molding handbook. 3rd ed*; 2000; Springer Science and Business Media New York, Chapter 1, pages 1-21.

[13] M. D. Hayat, G. Wen, M. F. Zulkifli, P. Cao; *Effect of PEG molecular weight on rheological properties of Ti-MIM feedstocks and water debinding behavior*; Powder Technology; vol. 270 (2015) pages 296–301

[14] G. Chen , P. Cao, G. Wen, N. Edmonds; *Debinding behaviour of a water soluble PEG/PMMA binder for Ti metal injection moulding*; Materials Chemistry and Physics, vol. 139 (2013) pages 557-565

[15] A. Simchi, F. Petzoldt, T. Hartwig, *An Approach for Assessment of Sintering Behavior of Co-injection Moulded PIM Feedstocks by Dilatometric Analysis*; Euro PM2005 Metal Injection Moulding.

[16] G. B. Dutra; M. Mulser; R.r Calixto; F. Petzoldt; *Investigation of material combinations processed via Two-Component Metal Injection Moulding (2C-MIM)*; Material Science Forums, vol. 727-728 , 2012; pages 248-253.

[17] F.S. Buffington, K. Hirano, M.Cohen , *Self diffusion in iron*, Acta Metallurgica, 1961, vol. 9, Issue 5, pages 434 – 439.

[18] M.Mulser, G. B. Dutra; J. Rager; F.Petzoldt; *Influence of a Mismatch in Shrinkage for Two-Component Metal Injection Moulding (2C-MIM)*; PM2010 World Congress-Powder Injection Moulding of composite Parts.

[19] A. Simchi , A. Rota , P. Imgrund; *An investigation on the sintering behavior of 316L and 17-4PH stainless steel powders for graded composites Materials*; Science and Engineering; 2006; vol. A 424 () 282–289

[20] Ph. Imgrund, Dr. A. Rota, L. Kramer; *Processing and properties of bi-material parts by micro metal injection moulding*; Fraunhofer Institute for Manufacturing and Advanced Materials (IFAM), D-28215 Bremen, Germany

[21] Ph. Imgrund,, A. Rota, A. Simchi. *Microinjection moulding of 316L/17-4PH and 316L/Fe powders for fabrication of magnetic–nonmagnetic bimetals*; Journal of materials processing technology; 2008; pages 259–264

[22] J. Kazior,M. Nykiel, T. Pieczonk, T. Marcu Puscasc, A. Molinari; *Activated sintering of P/M duplex stainless steel powders*; Journal of

Materials Processing Technology(2004); vol.157–158; pages 712–717

[23] <http://www.thermocalc.com/>

[24] G. Straffellini, A. Molinari: *Effetto della densità sulla resistenza a trazione delle leghe ferrose sinterizzate*, La Metallurgia Italiana, 2002, 31.

[25] S. Allain, J.-P. Chateau, O. Bouaziz, S. Migot, N. Guelton; *Correlations between the calculated stacking fault energy and the plasticity mechanisms in Fe–Mn–C alloys*; Materials Science and Engineering, vol. A 387–389 (2004) pages 158–162.

[26] P.J. Ferreira, P. Muellner ; *A thermodynamic model for the stacking fault energy*; Acta mater. Vol. 46, 1998; No. 13, pages. 4479±4484,

[27] G. Bonny, N. Castin, D. Terentyev; *Interatomic potential for studying ageing under irradiation in stainless steels: the FeNiCr model alloy*; Modelling and Simulation in Material Science and Engineering, 2013; vol. 21; Issue 8

[28] Powder Metallurgy Stainless Steels: *Processing, Microstructures, and Properties; Sintering and Corrosion Resistance*; ASM International. All Rights Reserved; Chapter 5 (pages 59-68)